Supporting Information

Deterministic Control of Sn^{3+} Valence and Electronic Phase Evolution in $AgSnSe_2$

Paribesh Acharyya,[1] Yukun Liu,[2] Shima Shahabfar,[2] Hengdi Zhao,[3] Yihao Wang,[3] Anuradha Bhogra,[3] Thomas San Ie,[1] Kodimana Ramakrishnan Pradeep,[1] Christos D Malliakas,[1] Juncen Li,[5] Lawrence Rhoads,[5] Yuelin Kuang,[5] Matthew A Grayson,[5] Vinayak P Dravid,[2] Duck Young Chung,[3] Christopher Wolverton,[2] Alexios P. Douvalis,*[,6] and Mercouri G Kanatzidis*[,1,3]

[1]*Northwestern University Department of Chemistry, Evanston, IL 60208 USA*

[2]*Department of Materials Science and Engineering, Northwestern University, Evanston, Illinois 60208, United States*

[3]*Materials Science Division, Argonne National Laboratory, Lemont, IL 60439 USA*

[4]*Deutsches Elektronen-Synchrotron DESY, Notkestr. 85, 22607 Hamburg, Germany*

[5]*Electrical & Computer Engineering, Northwestern University, Evanston, Illinois 60208, USA*

[6]*Department of Physics, University of Ioannina, Ioannina, 45110, Greece*

**Corresponding author: adouval@uoi.gr; m-kanatzidis@northwestern.edu*

Experimental Section

Materials

silver shots (Ag, ≥ 99.99%, Sigma Aldrich), tin balls (Sn, 99.999%, Sigma Aldrich), antimony shots (Sb, 99.999%, American Elements), and selenium shots (Se, ≥ 99.99%, Alfa Aesar) were used for synthesis without further purification.

Synthesis

Synthesis of $AgSn_{1-x}Sb_xSe_2$ (x =0 -0.99)

High quality polycrystalline ingots of $AgSnSe_2$ were synthesized by mixing appropriate ratio of starting element of Ag, Sn, and Se in a quartz tube (13 mm outer diameter, 11 mm inner diameter). The tubes were sealed under high vacuum (10^{-3} mbar) and slowly heated to 673 K over 12 h and then heated up to 1123 K over 4 h, soaked for 10 h and finally cooled down to room temperature over 10 h. Similar reaction procedure were followed for Sb doped/substituted $AgSnSe_2$ samples.

Synthesis of SnSe

High quality polycrystalline ingots of SnSe were synthesized by mixing appropriate ratio of starting element of Sn, and Se in a quartz tube (13 mm outer diameter, 11 mm inner diameter). The tubes were sealed under high vacuum (10^{-3} mbar) and slowly heated to 673 K over 12 h and then heated up to 1223 K over 4 h, soaked for 10 h and finally cooled down to room temperature over 10 h. The PXRD pattern of as-synthesized SnSe is shown in **Figure S25a.**

Synthesis of $SnSe_2$

High quality polycrystalline ingots of $SnSe_2$ were synthesized by mixing appropriate ratio of starting element of Sn, and Se in a quartz tube (13 mm outer diameter, 11 mm inner diameter). The tubes were sealed under high vacuum (10^{-3} mbar) and slowly heated to 673 K over 12 h and then heated up to 1323 K over 4 h, soaked for 10 h and finally cooled down to room temperature over 20 h. The PXRD pattern of as-synthesized SnSe is shown in **Figure S25b.**

Single crystal X-ray diffraction (SCXRD)

For the acquisition of intensity data, a suitable single crystal of $AgSn_{1-x}Sb_xSe_2$ (x =0 and 0.5) was mounted on a loop with paratone oil and mounted onto a XtaLAB Synergy Diffractometer. The XtaLAB Synergy diffractometer was equipped with a microfocus-sealed X-ray tube

PhotonJet (Mo) X-ray source and a Hybrid Pixel Array Detector (HyPix). The temperature of the crystals was controlled with an Oxford Cryosystems low-temperature device. Data reduction was performed with the CrysAlisPro software (Rigaku) using an empirical and numerical absorption correction. $AgSn_{1-x}Sb_xSe_2$ (x =0 and 0.5) was solved with the ShelXT[1] structure solution program using the intrinsic phasing solution method and by using Olex2[2] as the graphical interface. The model was refined with ShelXL[3] using least squares minimization. All crystal data from the SCXRD experiments can be found in **Tables S1-S8.**

Powder X-ray diffraction (PXRD)

PXRD patterns were obtained using a Rigaku Miniflex 5600 diffractometer with Cu Kα (λ = 1.5406 Å) radiation. The diffraction data were collected over a 2θ range of 5° to 90°, using a scan step size of 0.02° and a scanning rate of 10° per minute. Le Bail refinement was performed using the FullProf program.[4]

X-ray Pair Distribution Function (X-PDF)

Total scattering data for $AgSn_{1-x}Sb_xSe_2$ (x =0 and 0.5) were collected at room temperature. Each sample was loaded into a Kapton capillary (~1 mm in diameter) and mounted on a STOE StadiVari diffractometer equipped with an AXO Ag Kα microfocus sealed X-ray source A-MiXS, running at 65 kV and 0.68 mA, and a Dectris Pilatus3 R CdTe 300 K Hybrid Photon Counting detector. The data were integrated using the program GSAS-II. The total scattering structure function, *S(Q)*, was Fourier transformed to obtain the real-space pair distribution function, *G(r)*, using the program PDFgetX3.[5] PDF refinements were performed in PDFgui,[6] with structural models refined over an *r*-range of 2–20 Å. The goodness-of-fit (R_w) value for $AgSnSe_2$ and $AgSn_{0.5}Sb_{0.5}Se_2$ are 10.9 and 11% respectively.

Differential Thermal Analysis (DTA)

Thermogravimetric thermal analyses were performed in a Netzsch STA 449 F3 Jupiter Simultaneous Thermal Analysis (STA) instrument. ~10 mg of sample was sealed in a quartz ampule under vacuum (~3 x 10^{-3} mbar). DTA data was measured under Nitrogen gas (25 mL/min). The temperature was increased/decreased at a rate of 10 °C/min from room temperature to 900 °C. A similarly sealed ampule of ~50 mg of Al_2O_3 was used as a reference.

Optical band gap measurement

The optical band gap was determined by infrared spectroscopy instrument (Nicolet 6700 FT-IR spectrometer) in the mid-IR range (6000~400 cm^{-1}). The electronic energy band gaps were calculated based on the Kubelka-Munk relationship: $\alpha/S = (1-R)^2/2R$, where α and S are the absorption and scattering coefficients, respectively, and R is the reflectance.

X-ray photoelectron spectroscopy measurements (XPS)

XPS were performed using a Thermo Scientific Nexsa G2 system (monochromated Al Kα radiation, ~1486.6 eV) at a pressure of ~6.4×10^{-7} mbar and with an analysis spot size of 50 μm. Samples were charge compensated with a flood gun. The surface contamination was removed with Ar beam sputtering.

Scanning/transmission electron microscopy (S/TEM) analysis

High-resolution S/TEM (HR-S/TEM) imaging was conducted using an aberration-corrected JEM-ARM200F microscope (JEOL Ltd, Japan) operating at 200 kV. A condenser aperture was selected to provide a convergence semiangle of 27.5 mrad. Electron energy loss spectrum was acquired using a JEM-ARM300F (JEOL Ltd, Japan) operating at 300 kV equipped with a Gatan GIF Continuum K3 system. To prepare the electron-beam transmitted TEM specimens, the bulk samples were first ground and polished to a thickness of ~30 μm, followed by Ar-ion milling (3 kV for ~30 min until a hole was formed, and ion cleaning at 0.3 kV for 40 min at a low temperature (liquid nitrogen stage). Scanning electron microscopic (SEM) analyses were performed using a Schottky field-emission SEM (JEOL JSM-7900FLV SEM) at 20 kV.

Mössbauer spectroscopy

^{119}Sn Mossbauer spectra of the ground $AgSn_{1-x}Sb_xSe_2$ powder samples were collected at 80 K in transmission geometry, using a constant-acceleration Mössbauer spectrometer equipped with a $Ca^{119m}SnO_3$ source kept at RT and a variable-temperature liquid nitrogen bath cryostat (Oxford Instruments Variox 760). The spectrometer was calibrated with metallic iron at 80 K and the analyses of the spectra were performed by the IMSG code.[7] The isomer shift values are given relative to SnO_2 at room temperature (300 K).

For data fitting, we considered i) the relative literature on the $AgSnSe_2$ Mössbauer spectra analyses,[8-10] which suggest the use of a single-line (with zero quadrupole splitting QS=0) component (singlet) and ii) our XRD results and analyses, which suggest that the crystal structure of all samples adopts the FCC NaCl-type symmetry.

The obvious selection to use only two singlets to fit the Mössbauer spectra of the x≥0.5 samples gave appropriate fitting quality parameters [$\chi^2=\Sigma(y_{exp}-y_{fit})^2$] only for x=0.9 and 0.8, while for x=0.7 and 0.5 a third singlet was necessary to be included in the model to improve the fitting quality. Applying this three-singlets model to the MS of the lower x values samples down to x=0.1 gave adequate fitting results in all cases. All the fitted spectra are presented in **Figure 3b-e and Figure S9**. The resulting Mössbauer parameters from these fits are listed in **Table S10** and the plots of the IS and absorption area (AA) values as a function of x appear in **Figure S11**. The IS values of these three singlets indicate the simultaneous presence of Sn^{3+}, Sn^{2+} and Sn^{4+} species in the samples.

X-ray absorption measurements

The samples for X-ray absorption measurements were prepared by homogeneously mixing the powders with cellulose to achieve an X-ray absorption edge jump close to one, followed by pressing the mixture into pellets. X-ray absorption measurements were performed at the Sn K-edge (29.2 keV) on Beamline P65 at PETRA III, operating in transmission mode using gas ionization chambers filled with suitable gases. The incident X-ray photon energies were selected using a Si (311) double-crystal monochromator (DCM). For X-ray beam energy calibration, the transmission signal of a Sn reference foil was used. The beam size was set using slits to a dimension of 0.3 (vertical) × 1.5 (horizontal) mm^2.

Data were processed using Athena software by extracting the EXAFS oscillations χ(k) as a function of photoelectron wavenumber k following standard procedures.[11] The theoretical model and corresponding paths were generated using FEFF6 based on a calculated ordered CIF of $AgSnSe_2$. The fitting of the theoretical model to the experimental data was carried out using the fitting program Artemis with FEFF6 built into it.[11] To isolate the χ(k) oscillations, the atomic background was subtracted by applying a low distance cut-off equal to 1 Å in the Fourier transform and using a cubic spline. Fourier filtering was accomplished with a k weight equal to 2, ranging from 2 to ~10 $Å^{-1}$. Fitting parameters were obtained by modelling the EXAFS data of each sample in real(R)-space until a satisfactory global fit describing the system was obtained.

Heat capacity (C_p) measurement

Low-temperature heat capacity (C_p) of $AgSnSe_2$ was measured in a Quantum Design Dynacool Physical Property Measurement System (Dynacool-PPMS) in the temperature range of 2 - 300

K. A sample puck with the appropriate amount of Apiezon N grease was first measured as the background. The sample heat capacity was measured afterward by mounting a sample on top of the sample puck. The measurement was performed using a time relaxation method. We attempted to fit the low-temperature C_p data using the Debye–Einstein model:[12,13]

$$\frac{C_p}{T} = \gamma + \beta T^2 + \sum_n \left(A_n \left(\theta_{E_n}\right)^2 . (T^2)^{-3/2} . \frac{e^{\theta_{E_n}/T}}{\left(e^{\theta_{E_n}/T} - 1\right)^2} \right)$$

in which γ is Sommerfeld coefficient and accounts for electronic contribution. $\beta = C(12\pi^4 N_A k_B/5) \cdot (\Theta_D)^{-3}$ signifies the lattice contribution, where N_A, k_B and Θ_D are the Avogadro's number, Boltzmann constant and Debye temperature, respectively and C is defined as, $C = 1 - \sum_n A_n/3NR$, where N represents the number of atoms per formula unit and R denotes the universal gas constant (R = 8.314 J mol^{-1}K^{-1}). The third term in equation 1 describes the contributions of Einstein oscillators corresponding to the localized vibrations, where θ_{E_n} is the Einstein temperature for the n^{th} mode.

Electrical transport

Electrical conductivity and Seebeck coefficients of all the samples (2 X 2 X 8 mm^3) were measured simultaneously under a Helium atmosphere in an ULVAC-RIKO ZEM-3 instrument from room temperature to 673 K.

Low-temperature electrical resistivity measurements from 1.8 - 300 K were performed in a Quantum Design Dynacool Physical Property Measurement System (Dynacool-PPMS). Both DuPont 4929N-100 silver paint and H-20E silver epoxy were tested initially and were found to be undesirable, possibly due to the reaction between silver and the sample. After testing different ways of bonding wires (commercial solder, gallium, and indium), we conclude that indium is the best bonding agent to make electric contact. Standard four-lead methods were used to measure the longitudinal electrical resistivity (ρ_{xx}) with 25 μm thin gold wire bonded to the mirror-like surface via indium.

Hall measurement

Hall coefficient (R_H) was measured on a homemade apparatus. The Van der Pauw method was used on $\sim 5 \times 5 \times 0.3$ mm^3 plate samples. The Hall resistance was monitored by a Stanford Research System SR860 Lock-in amplifier at 13Hz for higher signal-to-noise level. Depending

on the sample, the magnetic field was chosen from 9 to 16 T, provided by a superconducting magnet. The Hall resistance at negative field was measured by switching to the Onsager conjugate pair. The Hall coefficient was calculated from $R_H = (R_{AC,BD}(B) - R_{BD,AC}(B))/2B$. The apparent charge carrier concentration is given by $\rho_H = \frac{1}{eR_H}$ assuming single carrier.

Magnetic susceptibility

The dc-magnetic susceptibility measurements from 1.8 - 300 K were performed in a superconducting quantum interference device (SQUID) from Quantum Design Magnetic Property Measurement System (MPMS-3).

Thermal transport

Thermal diffusivity (D) of the samples (~ 1 mm thickness) were measured in a Netzsch LFA-457 instrument in the temperature range 300−673 K under a Nitrogen atmosphere (**Figure S22)**. The total thermal conductivity (κ_{total}) was calculated using the formula κ_{total} = D X ρ X Cp where ρ is the density of the sample and Cp is the heat capacity of the sample. Here we have used Dulong−Petit's C_p value (0.25 J g^{-1} K^{-1})to calculate the κ_{total} of all the samples. The obtained density of all the samples is mentioned in **Table S18**. The error in thermal conductivity measurement is ~5%. To determine the lattice thermal conductivity of $AgSnSe_2$ ($\kappa_L = \kappa - \kappa_e$), the electronic contribution (κ_e, **Figure S24a**) was estimated using the Wiedemann–Franz law, $\kappa_e = L\sigma T$, where L is the temperature dependent Lorenz number.[14]

Computational details

First-principles calculations were performed within density functional theory (DFT) using the projector augmented wave (PAW)[15,16] method and the Perdew–Burke–Ernzerhof (PBE)[17] generalized gradient approximation (GGA)[18] as implemented in the Vienna Ab initio Simulation Package (VASP).[19,20] A plane-wave kinetic energy cutoff of 600 eV was used. All structures were relaxed until the residual forces on each atom were less than 0.1 meV/atom.

$AgSnSe_2$, $AgSbSe_2$, and Sn-doped $AgSbSe_2$ were modelled using special quasi-random structures (SQS) generated with the ICET package.[21] A 64-atom supercell was chosen to balance accuracy and computational cost. After full structural relaxation, electronic band structures were computed. Band unfolding was not performed, as the focus here is on

qualitative features of the electronic structure (e.g., metallic vs. semiconducting behavior) rather than detailed dispersion analysis.

Detailed thermoelectric Properties

Thermoelectric (TE) materials present a compelling avenue for sustainable energy technologies by enabling direct conversion of heat (particularly industrial or environmental waste heat) into electricity, all without the release of greenhouse gases or moving parts.[22-27]

$AgSnSe_2$ exhibits a superconductor to metal transition at ~ 5 K. So above 5 K, $AgSnSe_2$ exhibits metallic behaviour.[28] The room temperature σ is ~ 3056 S/cm (**Figure S19a).** Due to its high σ and carrier concentration (*n*) of ~ 2.4 x 10^{22} cm^{-3} (**Table S15**), $AgSnSe_2$ is used to enhance the σ of state-of-the-art TE materials like SnSe,[29] $Bi_{0.5}Sb_{1.5}Te_3$,[30] and many more.[31-34] Despite its promising electrical properties, the intrinsic TE performance of $AgSnSe_2$ itself remains largely unexplored. Notably, $AgBQ_2$-type compounds (B = Sb, Bi; Q = S, Se, Te) have garnered increasing attention as potential high-performance TE materials. These systems are known for their ultralow lattice thermal conductivity (κ_L), primarily attributed to the stereochemically active lone-pair electrons at the B-site cations.[23,35-39] While $AgSnSe_2$ shares the same ABX_2-type structural motif and exhibits compositional similarities with this class of materials, its TE behavior has not been studied in depth. This lack of understanding stems from uncertainties regarding its crystal structure, oxidation states, and electronic structure which are essential for optimizing TE performance. Therefore, a comprehensive structural and electronic investigation of $AgSnSe_2$ is crucial to unlocking its potential as a TE material. This motivates us to explore and improve its TE properties. For optimization, we systematically substitute Sb at the Sn site to tune its carrier concentration, as $AgSbSe_2$ is a well-known semiconductor with a room temperature σ of ~4.5 S/cm.[40]

We synthesized a series of polycrystalline $AgSn_{1-x}Sb_xSe_2$ compounds (x = 0-0.99) to explore their TE performance. The corresponding powder X-ray diffraction (PXRD) patterns are shown in **Figure S10**. With increasing Sb content, the diffraction peaks gradually shift toward lower angles, leading to lattice expansion. This systematic shift confirms the successful incorporation of Sb into the crystal structure. A similar systematic shift in diffraction peaks was also observed by the Zybala group.[41] Differential thermal analysis (DTA) of $AgSnSe_2$ revealed a melting point at 555 °C and recrystallization peak at 527 °C (**Figure S20a**). Post-DTA PXRD patterns showed no evidence of any structural transformation (**Figure S20b**). Therefore, the TE properties of all samples were measured up to 400 °C, which is well below the observed melting point.

Figure S19 illustrates the TE properties of $AgSn_{1-x}Sb_xSe_2$ compounds (x = 0-0.99). The temperature-dependent σ of $AgSnSe_2$ shows metallic behavior in the temperature range of 300-673 K, decreasing with increasing temperature (**Figure S19a**). Due to this metallic conductivity (σ is ~ 3056 S/cm at 300 K), no optical band gap could be detected within the measured energy range of 0.1-0.8 eV (**Figure S21**). With increasing Sb content, the σ gradually decreases, as shown in **Figure S19a**. Interestingly, at 40% Sb substitution, the system exhibits semiconducting behavior, whereas compositions with Sb content below 40% retain metallic-like conductivity. Beyond this threshold, the samples clearly show semiconducting-like transport characteristics. The unusually high σ of $AgSnSe_2$ can be attributed to the presence of Sn in the +3 oxidation state (**Figure 3a,b,f**), corresponding to an average $5s^1$ electronic configuration that facilitates charge delocalization. To highlight this behavior, we compared the σ of $AgSnSe_2$ with that of SnSe and $SnSe_2$, which exhibit significantly lower σ due to their stable Sn^{2+} ($5s^2$) and Sn^{4+} ($5s^0$) states, respectively. Furthermore, substituting Sn with Sb in $AgSn_{0.5}Sb_{0.5}Se_2$ suppresses the conductivity, as Sn tends to exhibit +2 and +4 oxidation states rather than +3 under such substitution (**Figure 3e**), as evident by the Mössbauer spectroscopy results. These comparisons, as shown in **Table S16** underscore the crucial role of Sn^{3+} in enabling metallic transport in $AgSnSe_2$. Correspondingly, the room temperature S of $AgSnSe_2$ is extremely low (~0.08 μV/K), and it increases modestly with temperature, reaching a maximum of ~5 μV/K at 673 K (**Figure S19b**), consistent with its metallic nature. Upon increasing Sb content, S increases significantly which is an indicative of a gradual transition from metallic to semiconducting behavior. Notably, $AgSn_{0.01}Sb_{0.99}Se_2$ exhibits a very high S of ~737 μV/K at 300 K. The temperature dependence of S further supports this transition: in $AgSn_{1-x}Sb_xSe_2$ (x = 0–0.4), S increases with temperature, as expected for metals or degenerate semiconductors,[42] while for $x > 0.4$, S decreases with temperature a characteristic signature of intrinsic semiconductors.[43] The corresponding power factor (σS^2) is shown in **Figure S19c**.

To gain insights into how Sb substitution influences the thermal transport in $AgSnSe_2$, we measured the temperature-dependent κ of $AgSn_{1-x}Sb_xSe_2$ (x = 0–0.99), as shown in **Figure S19d.** A clear trend of decreasing κ with increasing Sb content is observed. While pristine $AgSnSe_2$ exhibits a room-temperature κ of 2.8 W/m·K, heavy Sb substitution leads to a drastic reduction, reaching as low as 0.5 W/m·K for $AgSn_{0.01}Sb_{0.99}Se_2$ highlighting the strong impact of chemical tuning on phonon transport. As a result, a moderate zT of ~ 0.5 is achieved for the $AgSn_{0.01}Sb_{0.99}Se_2$ sample (**Figure S23**). The κ_L of $AgSnSe_2$ samples is illustrated in **Figure S24b.** The κ_L of $AgSnSe_2$ is ~1 W/m·K at room temperature and decreases with increasing temperature, a trend characteristic of crystalline solids.[44,45] Further to understand the

experimentally observed low κ_L in $AgSnSe_2$, we measured the heat capacity (C_p) in the temperature range of 2–300 K (**Figure S17**). The C_p data in the 2–47 K range were fitted using a Debye–Einstein model (**Figure S17c**) incorporating three Einstein modes (see methods and **Table S17**).[12,13] The Debye temperature is 202 K and three Einstein temperature are 122 K (85 cm^{-1}), 23 K (16 cm^{-1}), and 62 K (43 cm^{-1}) as mentioned in **Table S17**. Further a distinct peak near 10 K is observed in the C_p/T^3 versus T plot (inset of **Figure S17c**), similar to features reported in other low-κ_L materials.[46,47] This anomaly is indicative of an excess phonon density of states present in $AgSnSe_2$. These low-energy optical phonons interact strongly with acoustic heat-carrying modes, thereby suppressing phonon transport and contributing to the intrinsically low κ_L in this compound. Additionally, a distinct anomaly near 4.5 K marks the superconducting transition temperature underscoring the complex interplay between lattice dynamics and electronic ground states in $AgSnSe_2$.

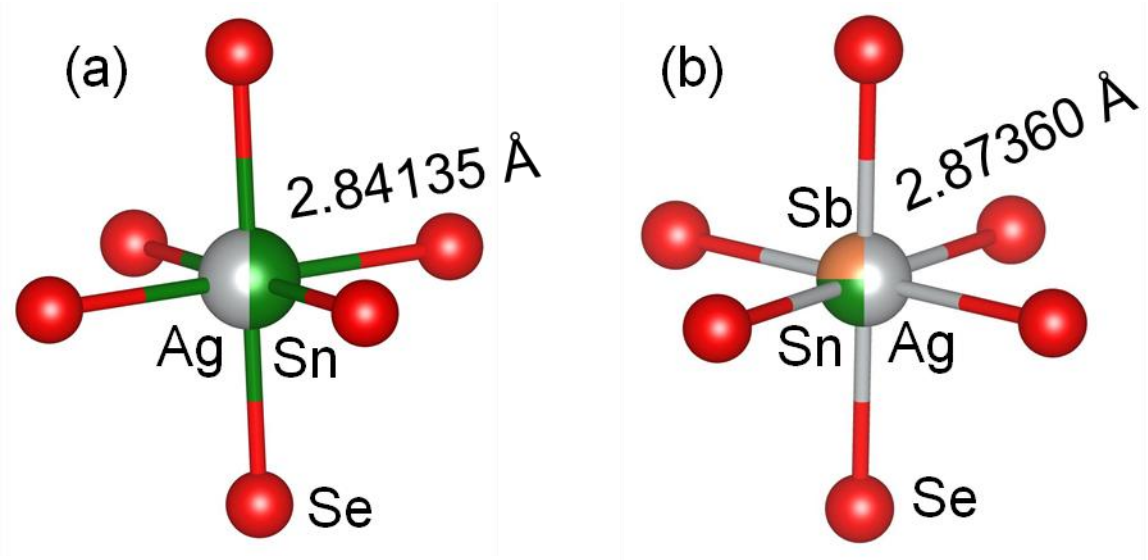

Figure S1. Octahedral unit of (a) $AgSnSe_2$ and (b) $AgSn_{0.5}Sb_{0.5}Se_2$. Ag, Sn, Sb and Se atoms are denoted by the grey, blue, orange and green spheres respectively.

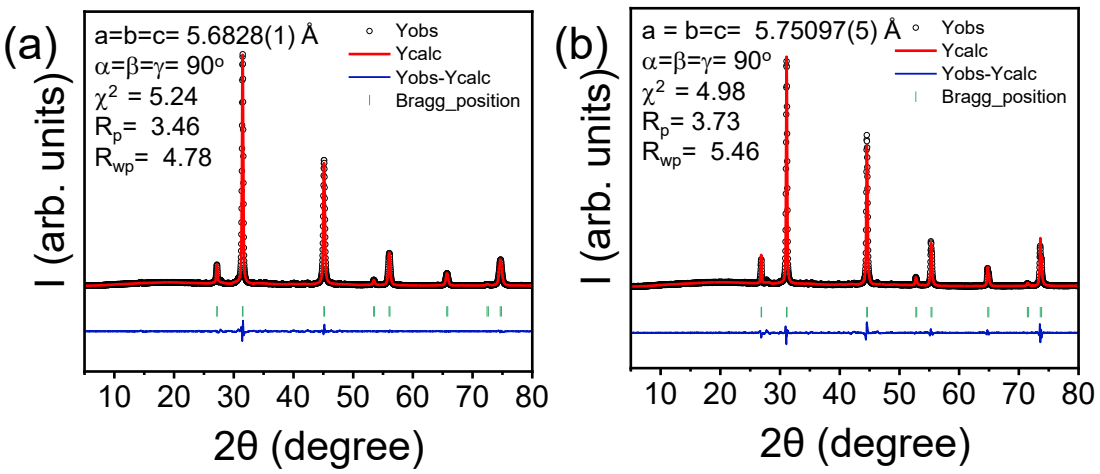

Figure S2. Le Bail refinement of the structural model of (a) $AgSnSe_2$ and (b) $AgSn_{0.5}Sb_{0.5}Se_2$ from the powder X-ray diffraction data recorded at room temperature.

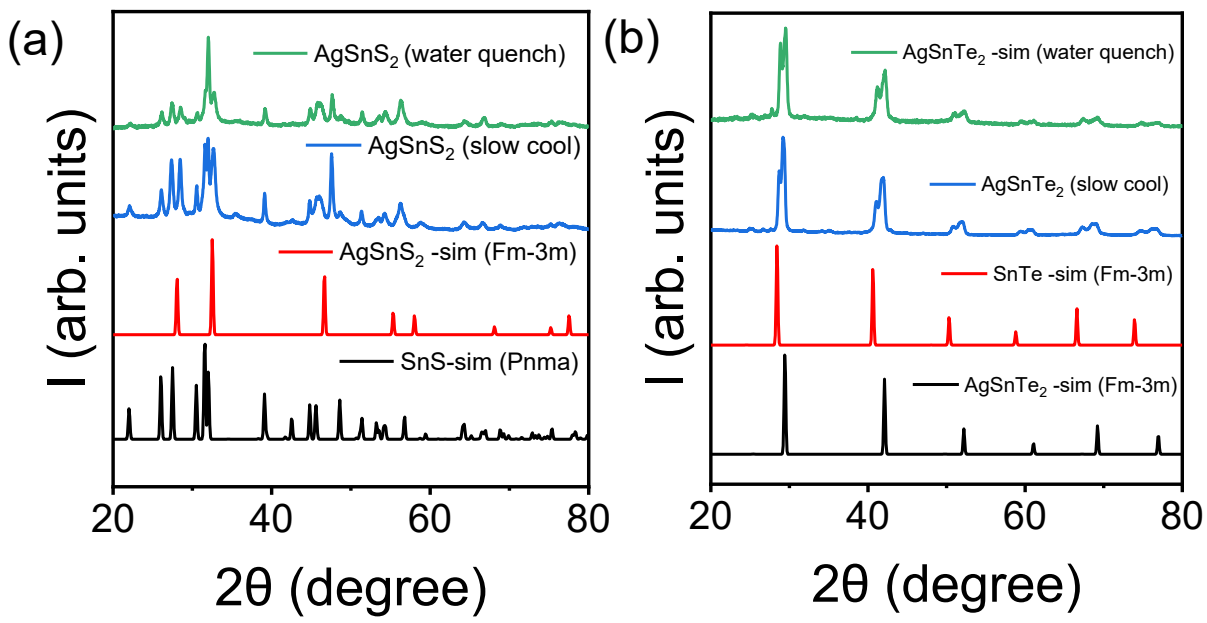

Figure S3. Powder X-ray diffraction data of $AgSnS_2$ and $AgSnTe_2$ recorded at room temperature. "slow cool" refers to samples cooled gradually from 850 °C, while "water quench" indicates quenching the sample from 850 °C directly into water to rapidly cool it.

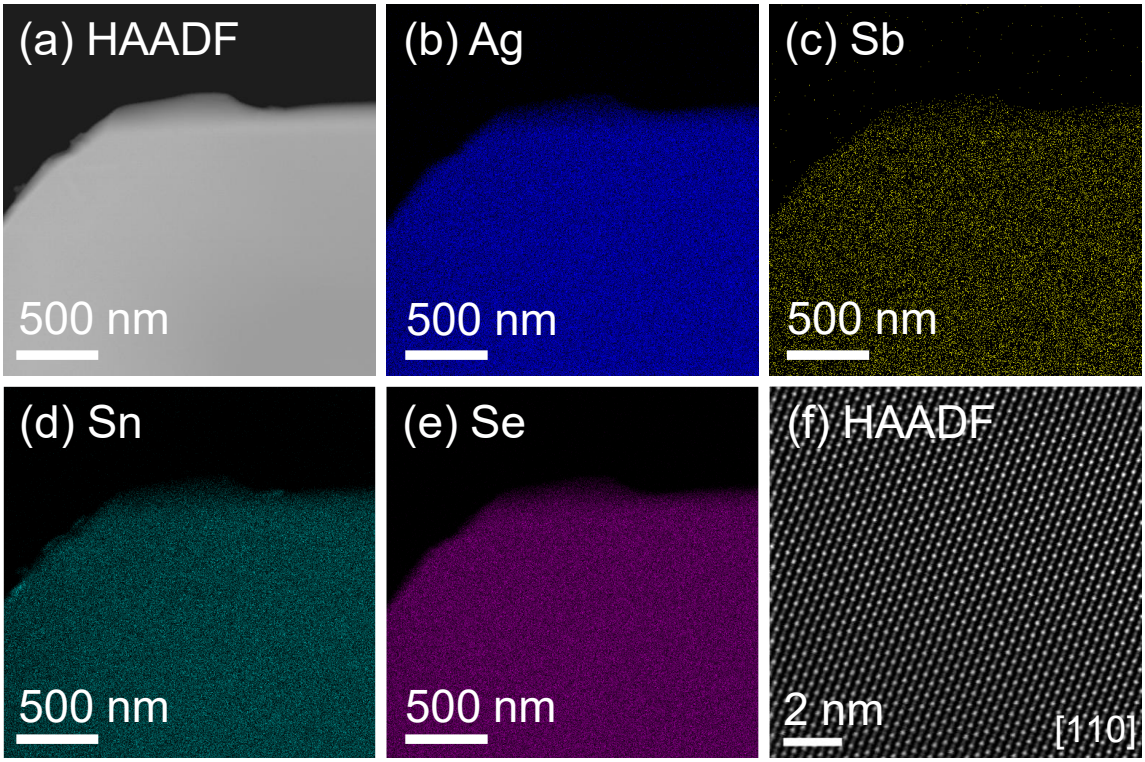

Figure S4. Scanning transmission electron microscopy (STEM) characterization of the $AgSn_{0.5}Sb_{0.5}Se_2$ microstructure. (a) High-angle annular dark-field (HAADF) image. Energy-dispersive X-ray spectroscopy (EDS) elemental maps of (b) Ag, (c) Sb, (d) Sn, and (e) Se. (f) Atomic-resolution HAADF images acquired along the [110] zone.

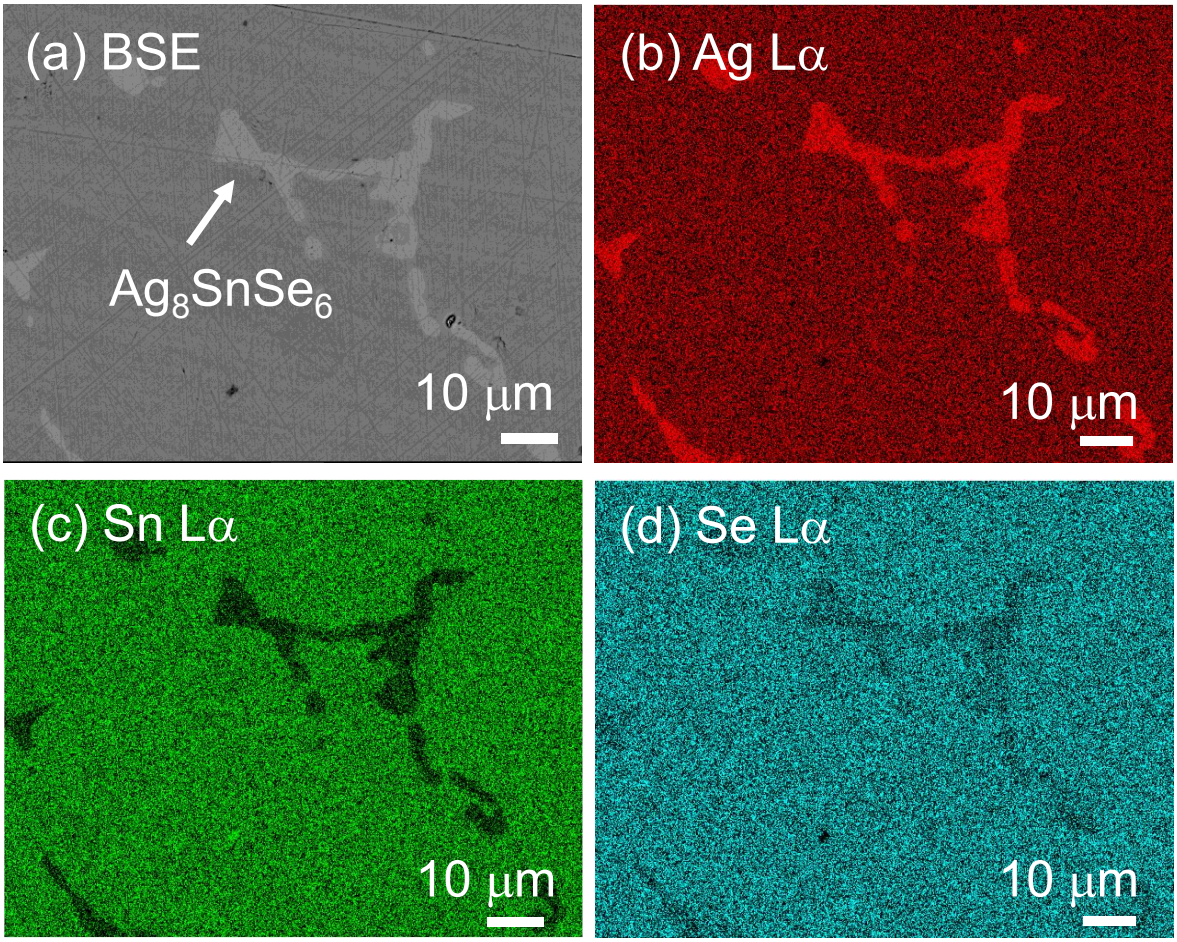

Figure S5. Scanning electron microscopy analysis on the microstructure of $AgSnSe_2$. (a) Backscattered electron (BSE) image. Energy dispersive spectroscopy map of (b) Ag, (c) Sn, and (d) Se.

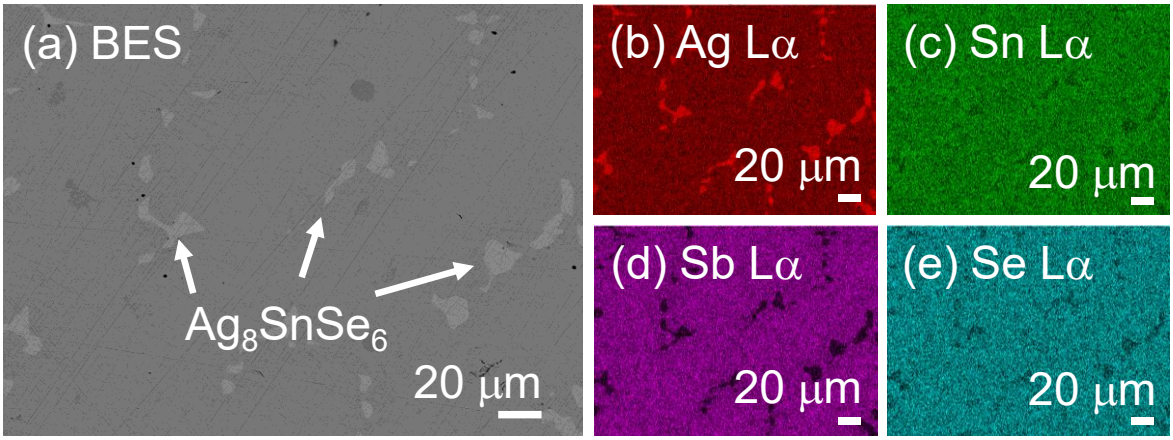

Figure S6. Scanning electron microscopy analysis on the microstructure of $AgSn_{0.5}Sb_{0.5}Se_2$. (a) Backscattered electron (BSE) image. Energy dispersive spectroscopy map of (b) Ag, (c) Sn, (d) Sb, and (d) Se.

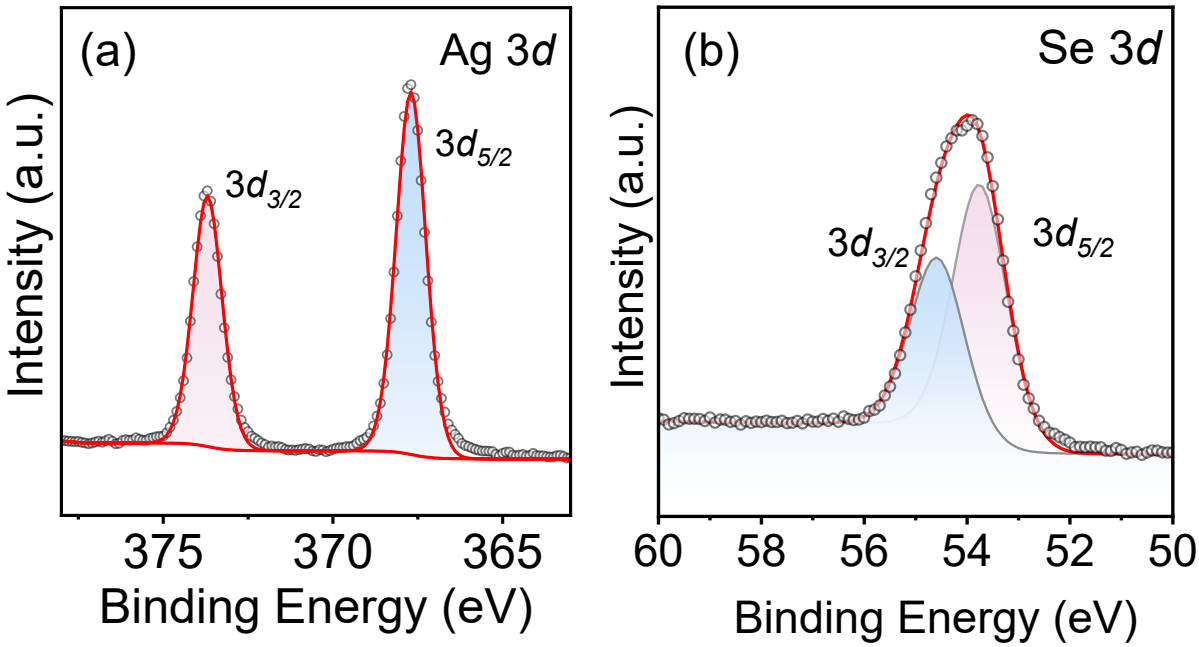

Figure S7. Photoemission spectra of (a) Ag 3d and (b) Se 3d for $AgSnSe_2$ measured with the photon energy of 1486.6 eV.

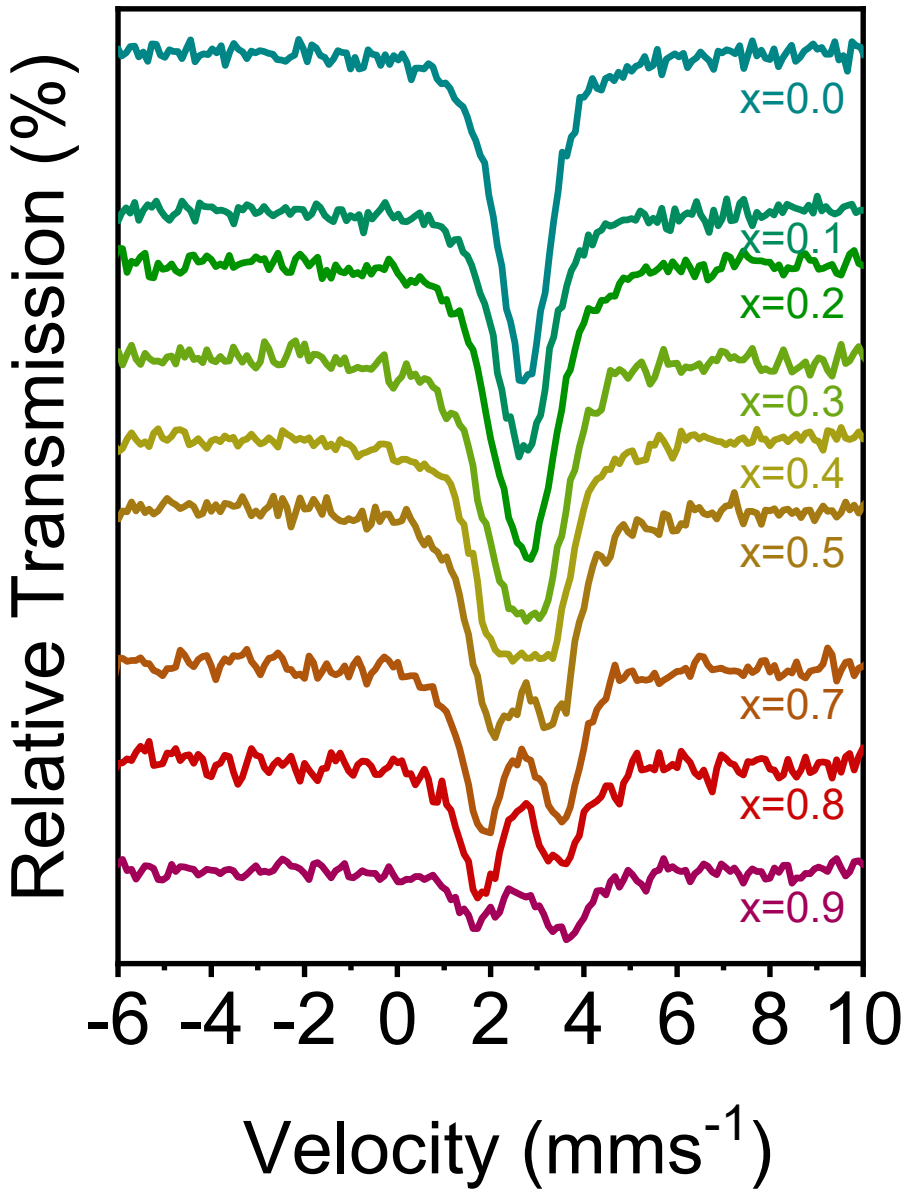

Figure S8. 80 K raw ^{119}Sn Mössbauer spectra of $AgSn_{1-x}Sb_xSe_2$.

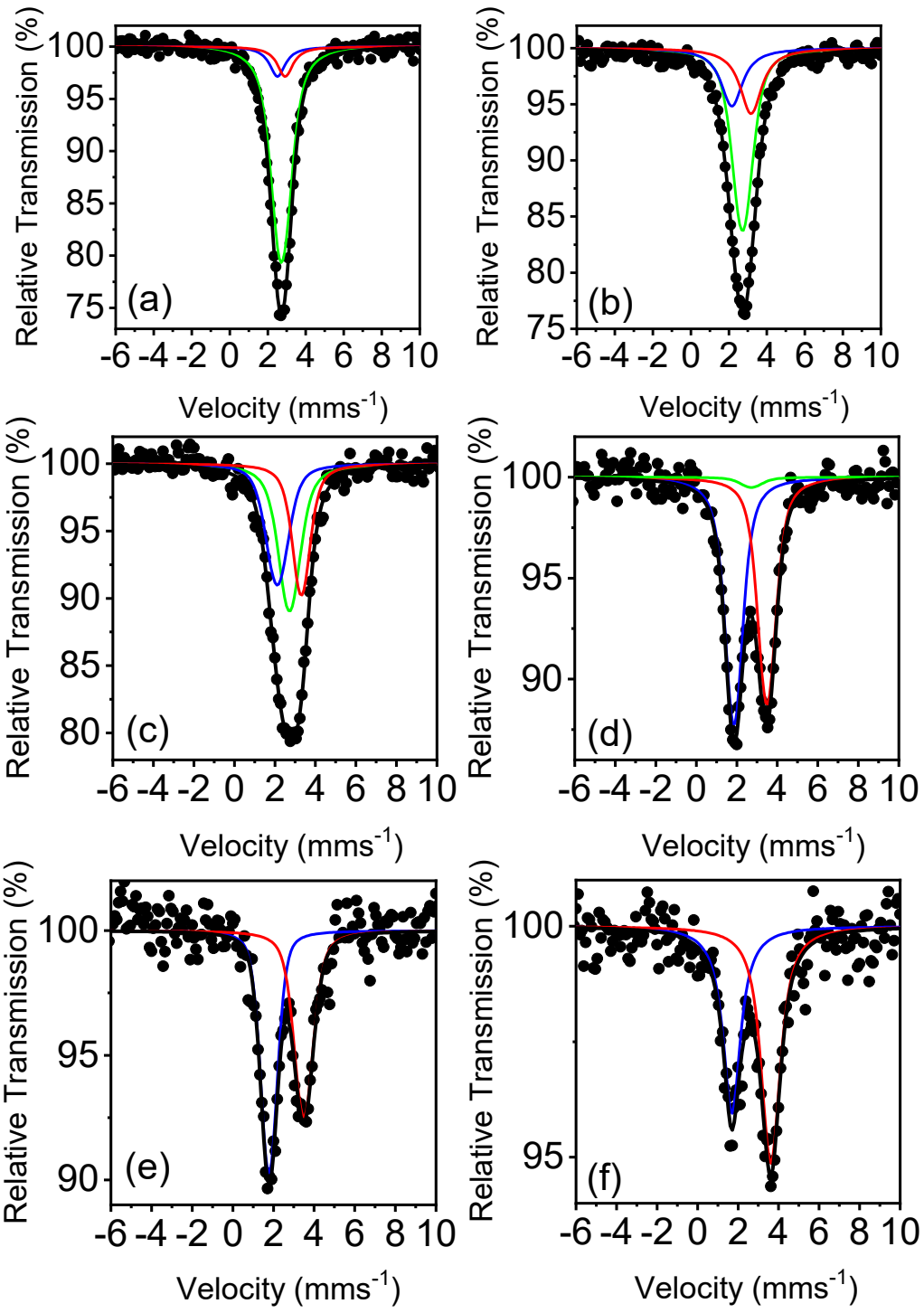

Figure S9. 80 K 119Sn Mössbauer spectra of AgSn1-xSbxSe2, (a) x = 0 (three-component), (b) x = 0.2, (c) x = 0.3, (d) x=0.7, (e) x=0.8, (f) x=0.9. The points correspond to the experimental data and the continuous lines to the components used to fit the spectra, blue for Sn4+, green for Sn3+ and red for Sn2+.

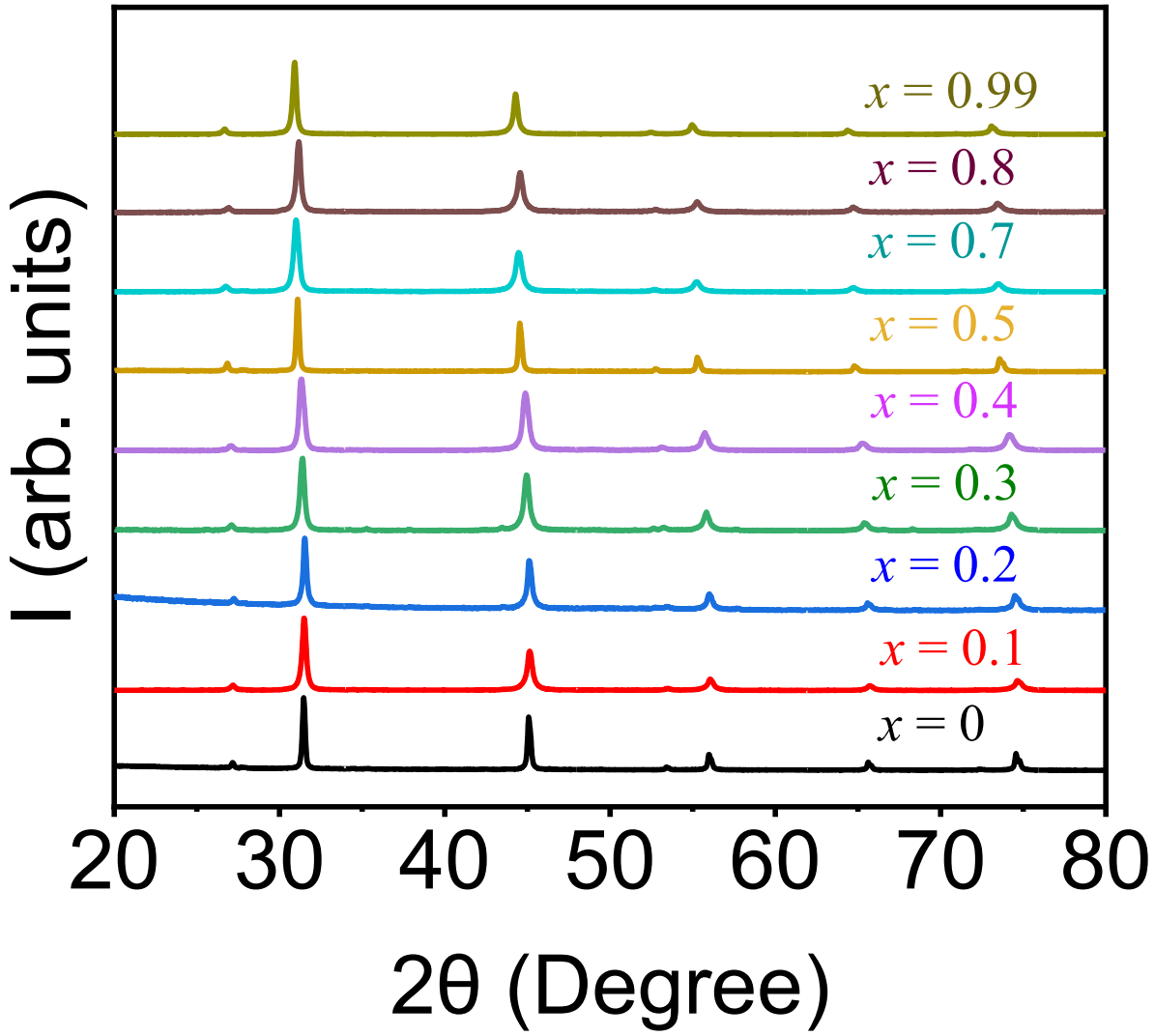

Figure S10. Room-temperature powder XRD patterns of $AgSn_{1-x}Sb_xSe_2$ (x = 0 -0.99) samples.

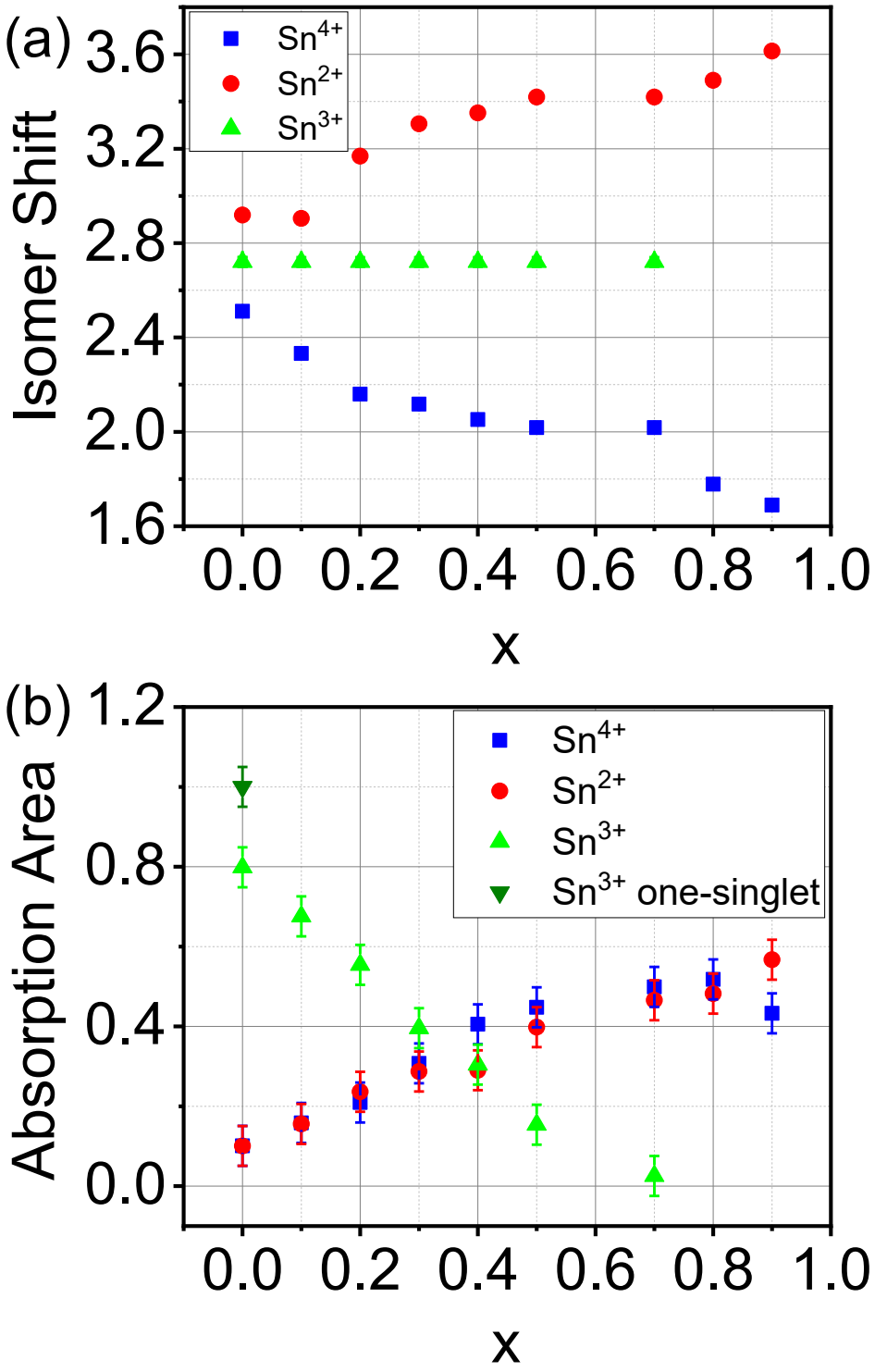

Figure S11. (a) Isomer shift and (b) absorption area of the components used to fit the 80 K ^{119}Sn Mössbauer spectra of $AgSn_{1-x}Sb_xSe_2$.

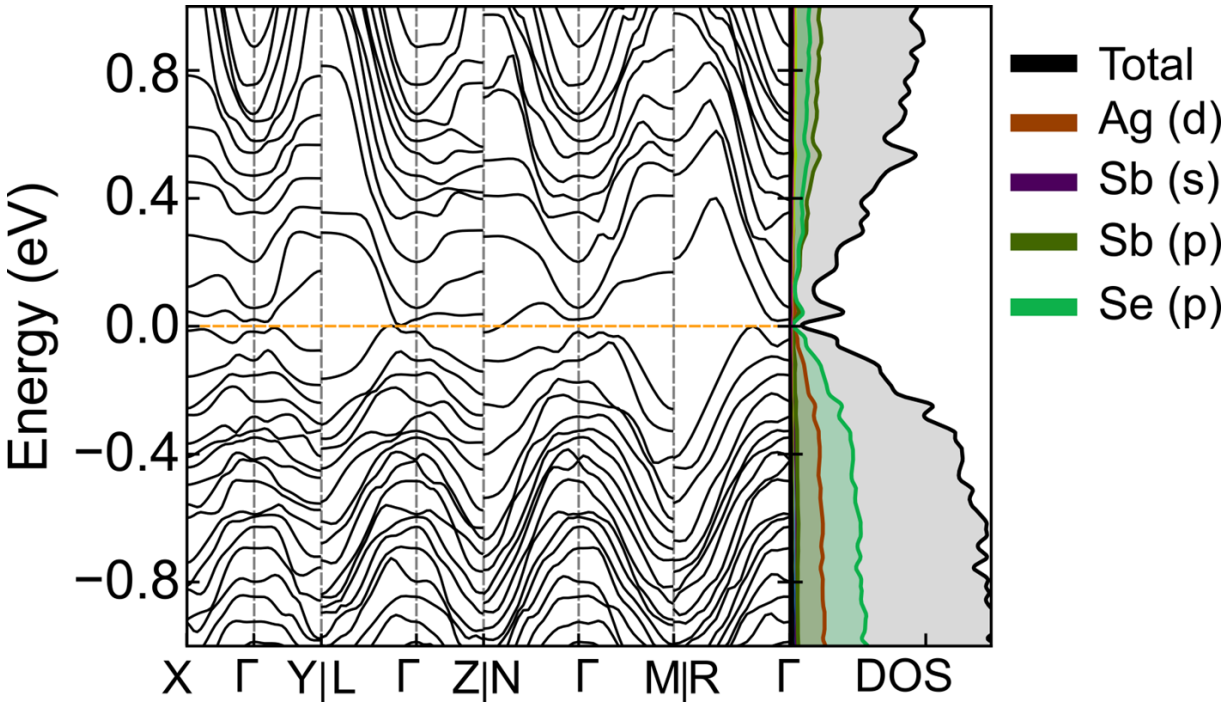

Figure S12. Electronic structures of $AgSbSe_2$.

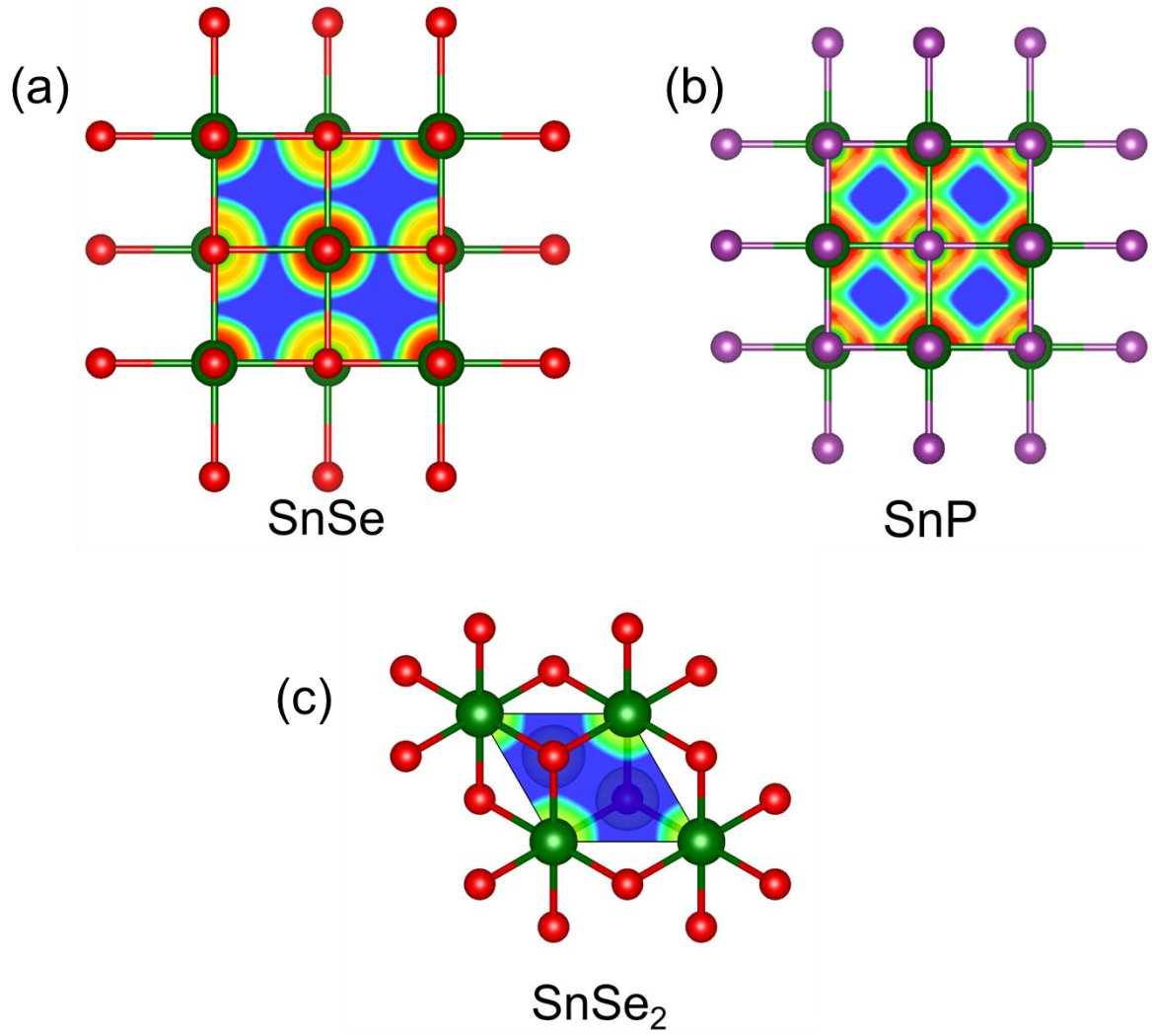

Figure S13. Electron localization function (ELF) visualized at an iso-surface value of 0.85 of the maximum charge density for (a) SnSe, (b) SnP and (c) $SnSe_2$. Sn, Se and P atoms are denoted by the green, red, and violet spheres, respectively.

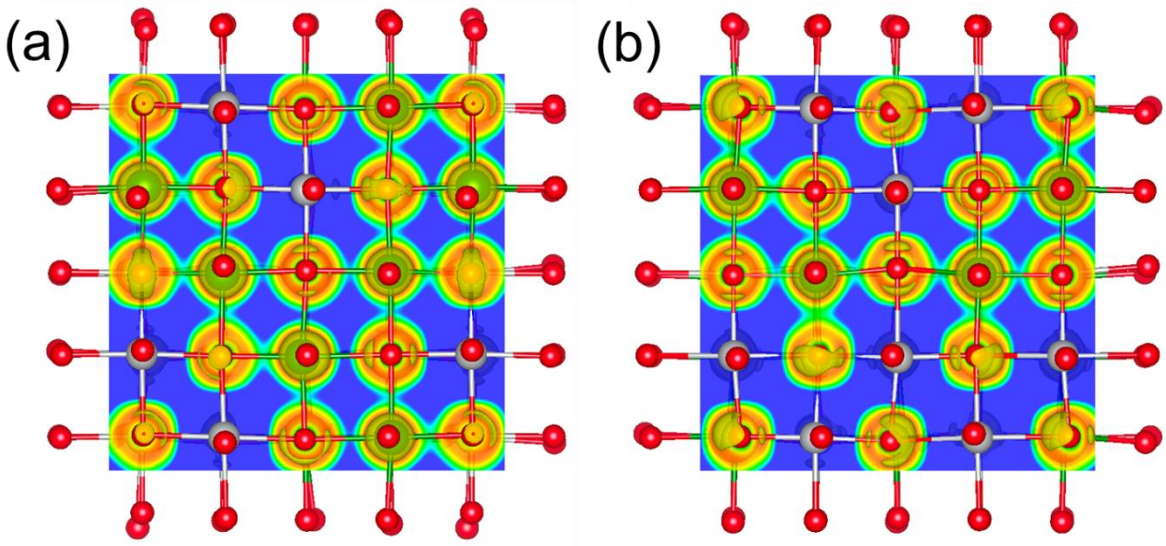

Figure S14. Electron localization function (ELF) visualized at an iso-surface value of 0.85 of the maximum charge density for $AgSnSe_2$ (a) along 001 direction and (b) 010 direction. Ag, Sn, and Se atoms are denoted by the grey, green, and red spheres, respectively.

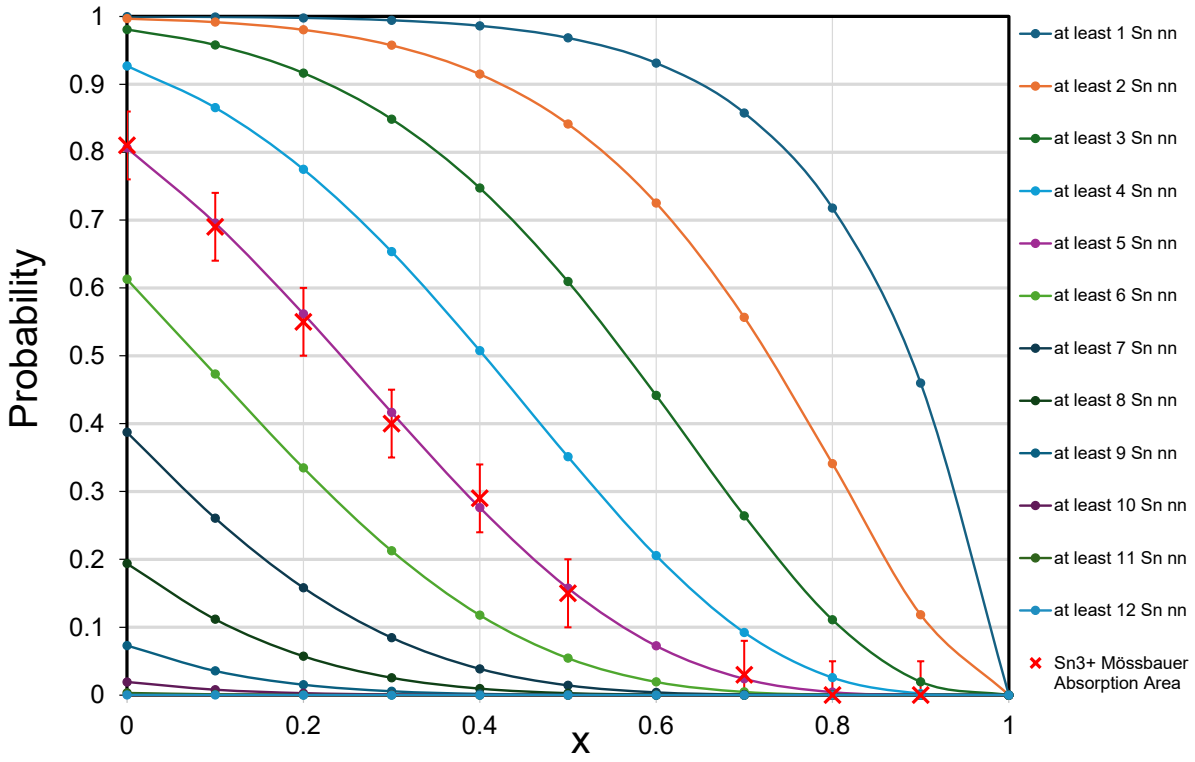

Figure S15. Plots of the total binomial probability of finding at least m and up to 12 first Sn cationic neighbors to a Sn site as a function of x in $AgSn_{1-x}Sb_xSe_2$ (continuous line + symbol curves) together with the plot of the absorption area of the Sn^{3+} component resulting from the fits of the corresponding Mössbauer spectra (red x symbols with error bars).

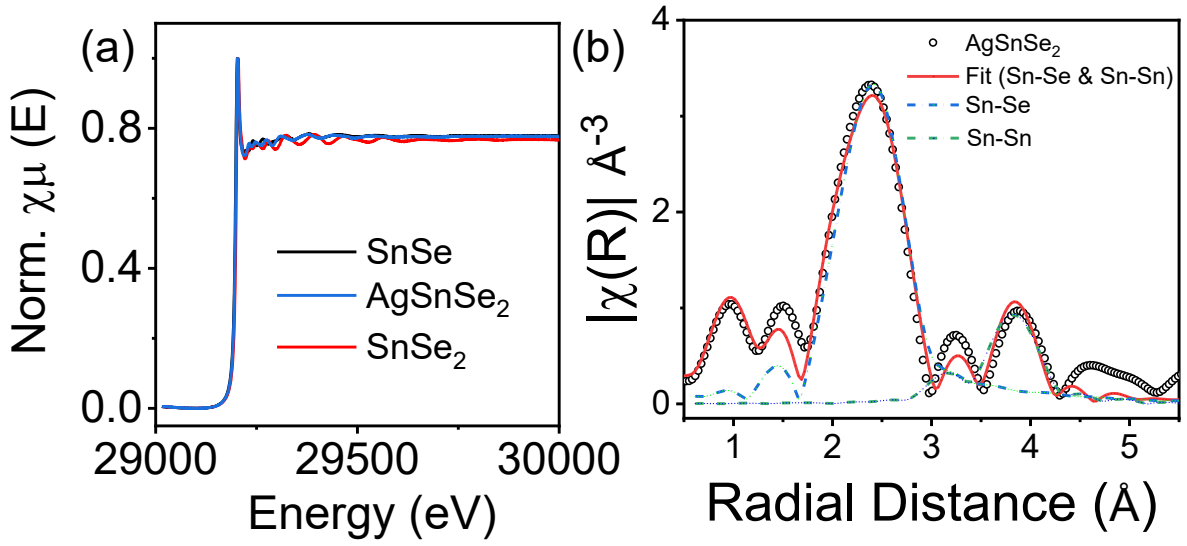

Figure S16. (a) Full-range Sn K-edge XANES spectra of SnSe, $AgSnSe_2$, and $SnSe_2$ showing overall spectral features across the energy range. (b) Magnitude of Fourier-transformed Sn-K-edge EXAFS spectra (open symbols) and their best fit (solid line) for $AgSnSe_2$. Dashed lines show their component fitting paths.

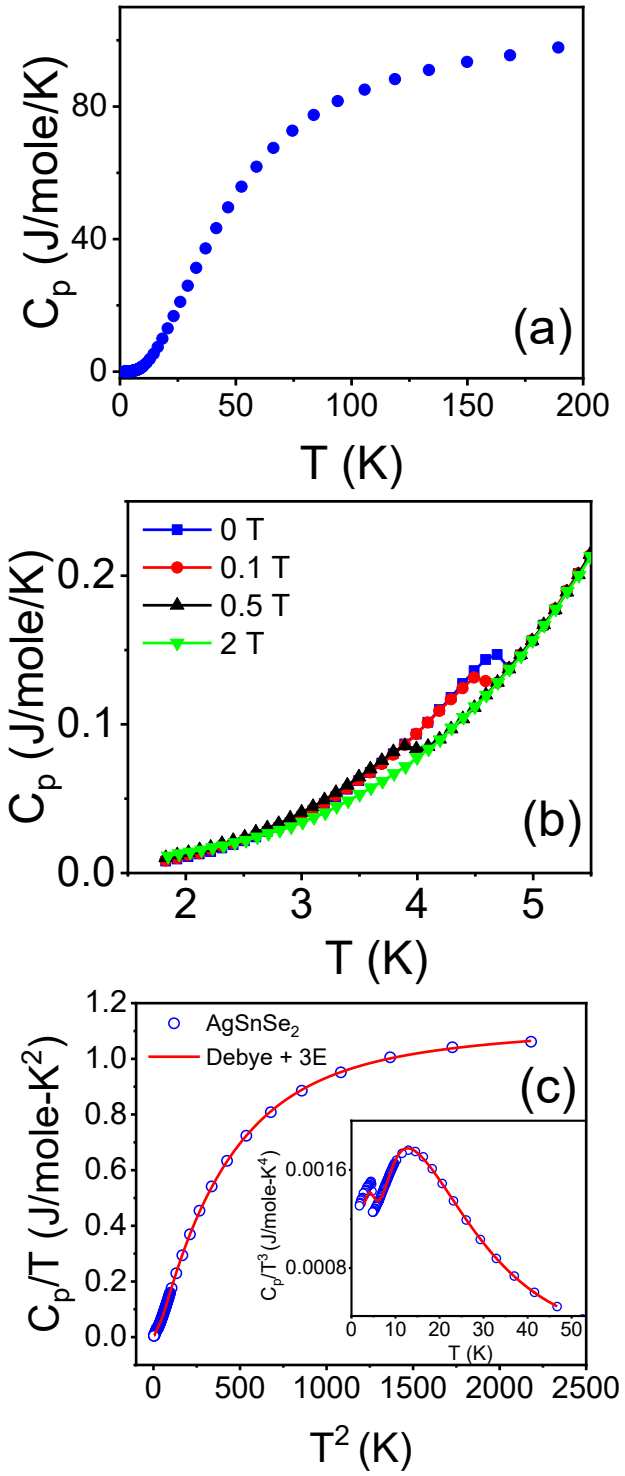

Figure S17. Heat capacity (C_p) of $AgSnSe_2$ of (a) C_p *vs.* T, and (b) enlarged view of the low-temperature region highlighting the magnetic field dependence. Low-temperature C_p/T versus T^2 plot of $AgSnSe_2$ and fit with Debye–Einstein model. Inset shows the C_p/T^3 vs. T plot.

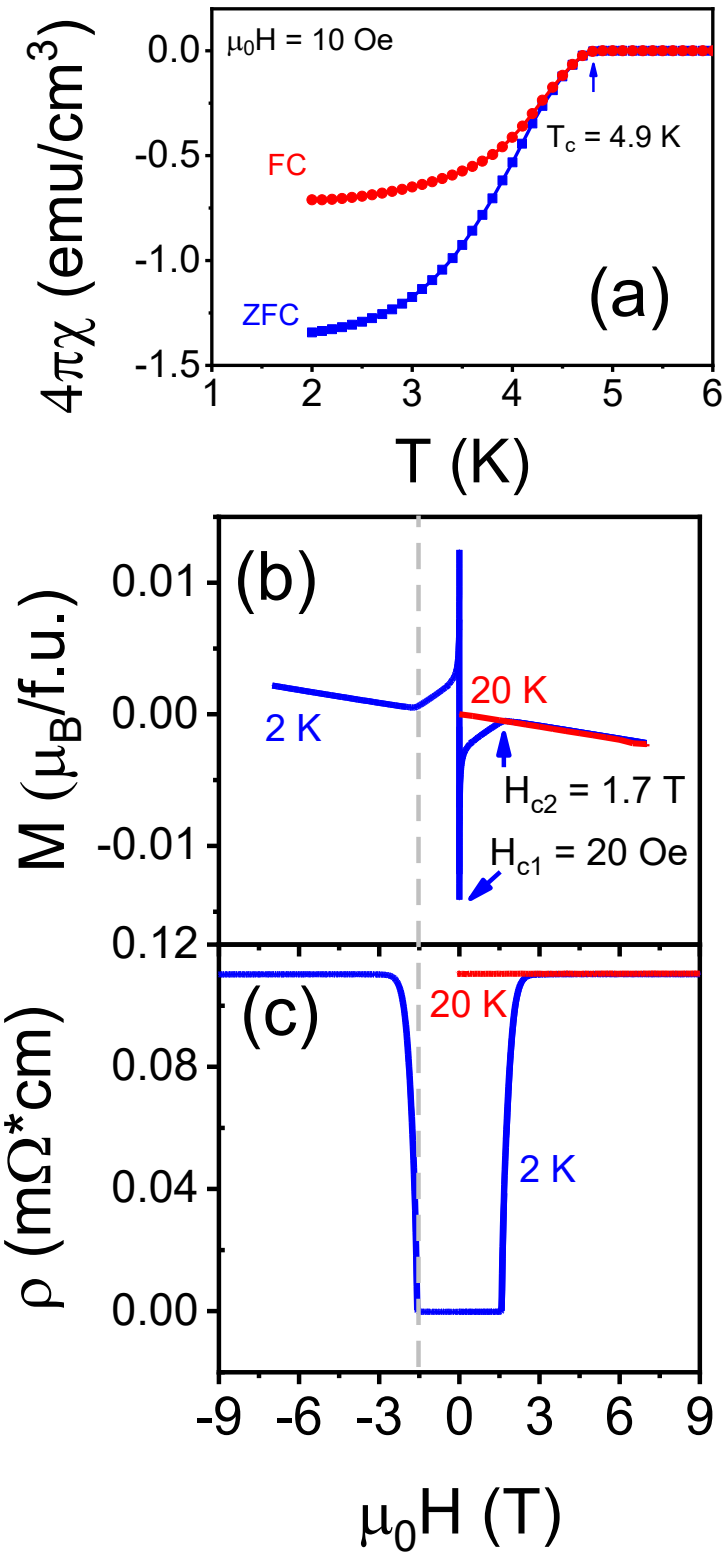

Figure S18. (a) Field-cooled (FC) and zero-field-cooled (ZFC) magnetic susceptibility, (b) the isothermal magnetization, and (c) magnetoresistance for $AgSnSe_2$.

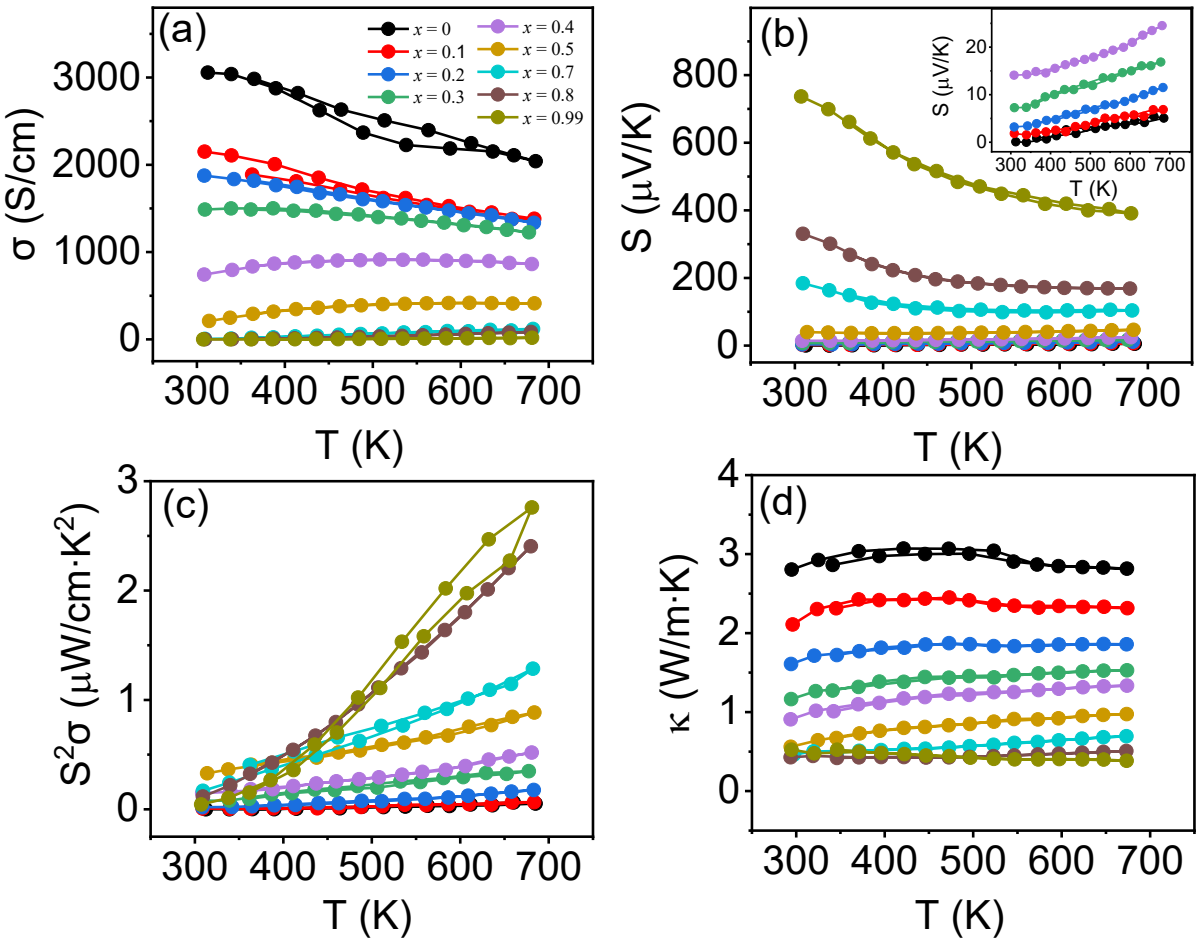

Figure S19. Temperature-dependent (a) electrical conductivity (σ), (b) Seebeck coefficient (S), (c) power factor (σS^2), and (d) total thermal conductivity, κ of $AgSn_{1-x}Sb_xSe_2$ (x = 0-0.99).

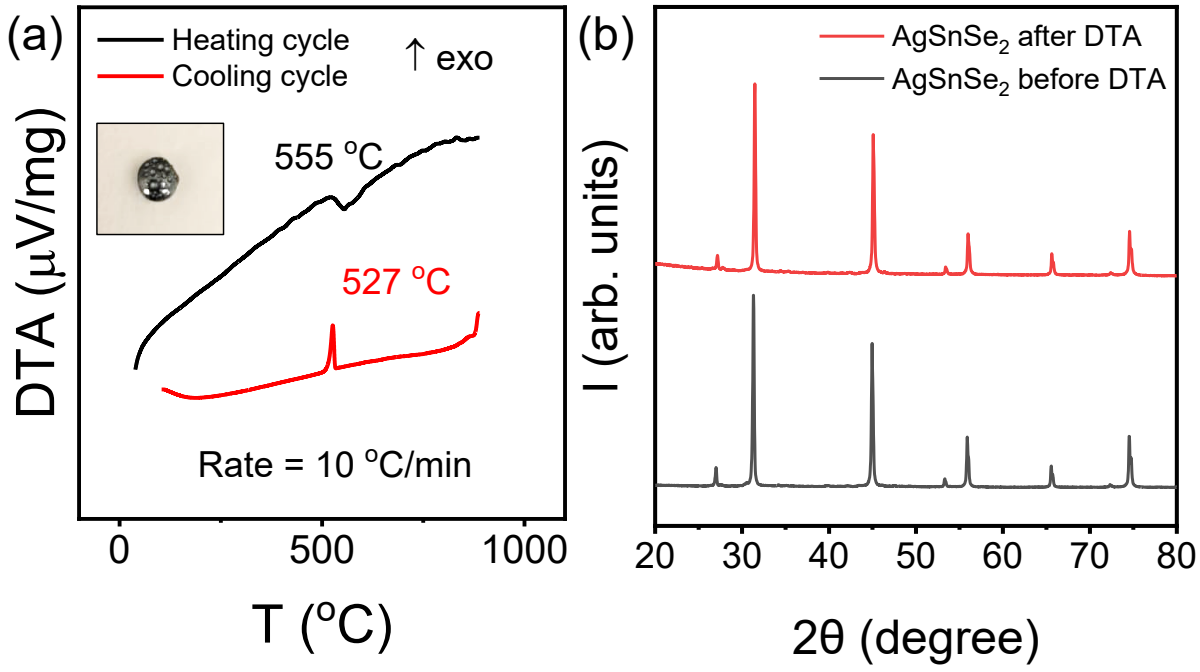

Figure S20. Differential thermal analysis (DTA) of (a) $AgSnSe_2$ showing one endothermic event upon heating at 555 °C and one exothermic (exo) event upon cooling at 527 °C. Inset: Photograph of the sample after DTA, (b) PXRD taken before and after DTA shows that the material was fully recovered.

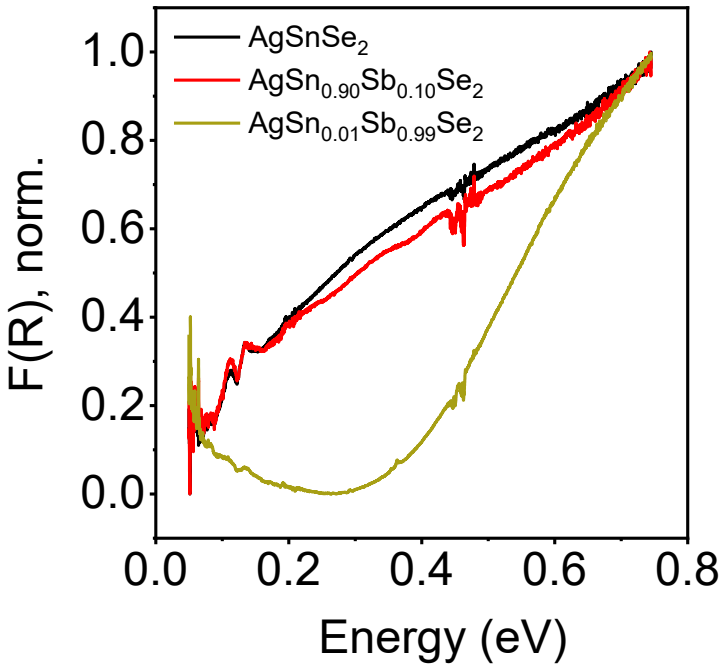

Figure S21. Optical absorption spectra of $AgSn_{1-x}Sb_xSe_2$ (x = 0, 0.1 and 0.99).

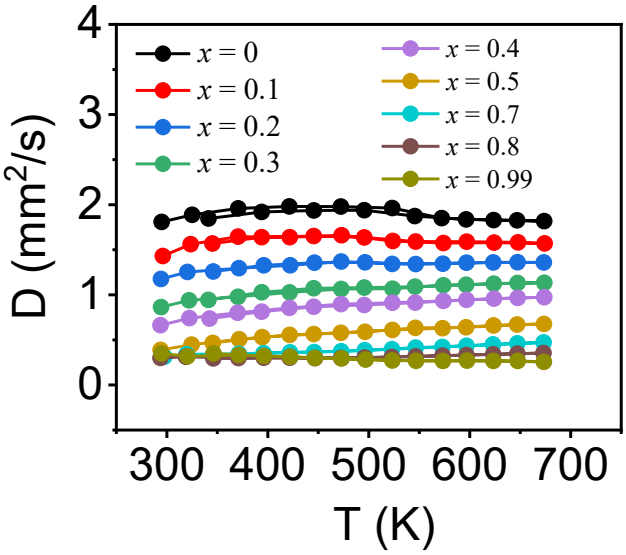

Figure S22. Temperature dependent diffusivity (D) of $AgSn_{1-x}Sb_xSe_2$ (x = 0–0.99) samples.

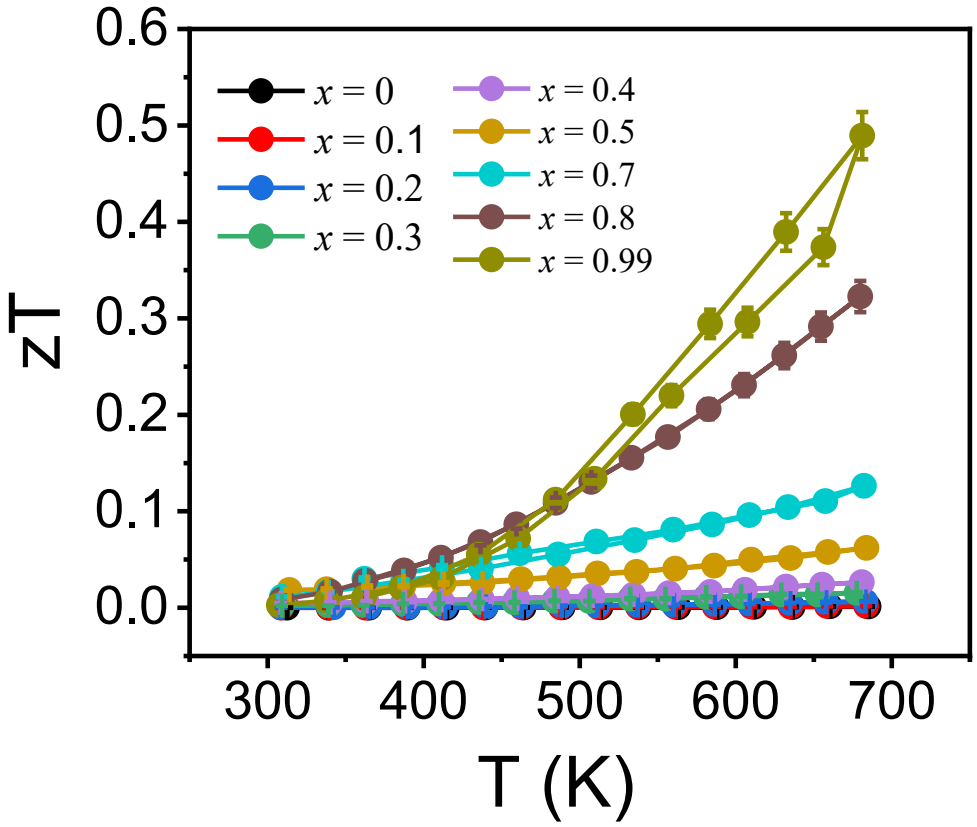

Figure S23. Thermoelectric figure of merit (zT) of $AgSn_{1-x}Sb_xSe_2$ (x = 0-0.99) samples.

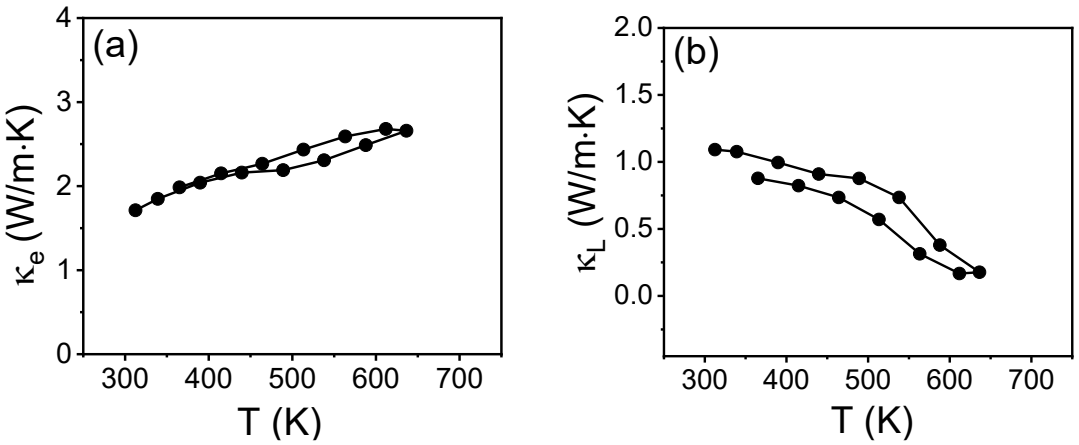

Figure S24. Temperature dependent electrical thermal conductivity (κ_e) and lattice thermal conductivity (κ_L), for $AgSnSe_2$ sample.

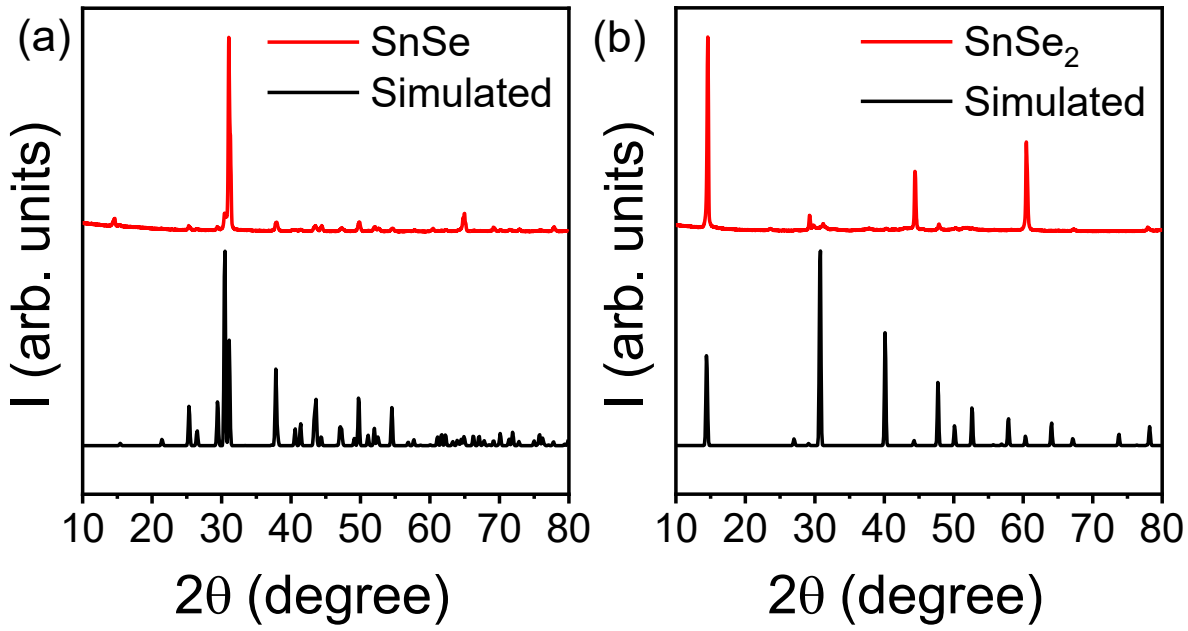

Figure S25. Room temperature powder X-ray diffraction pattern of (a) SnSe and (b) $SnSe_2$.

Table S1. Crystal data and structure refinement for $AgSnSe_2$ at 296.7(6) K.

Empirical formula	Ag Sn Se_2
Formula weight	384.48
Temperature	296.7(6) K
Wavelength	0.71073 Å
Crystal system	Cubic
Space group	*Fm*-3*m*
Unit cell dimensions	a = 5.6827(2) Å, α = 90° b = 5.6827(2) Å, β = 90° c = 5.6827(2) Å, γ = 90°
Volume	183.512(19) $Å^3$
Z	2
Density (calculated)	6.958 g/cm^3
Absorption coefficient	31.704 mm^{-1}
F(000)	330
Crystal size	0.124 x 0.124 x 0.031 mm^3
θ range for data collection	6.218 to 33.036°
Index ranges	-8<=h<=7, -8<=k<=5, -7<=l<=8
Reflections collected	389
Independent reflections	33 [R_{int} = 0.0478]
Completeness to θ = 25.242°	100%
Refinement method	Full-matrix least-squares on F^2
Data / restraints / parameters	33 / 0 / 4
Goodness-of-fit	1.081
Final R indices [I > 2σ(I)]	R_{obs} = 0.0097, wR_{obs} = 0.0249
R indices [all data]	R_{all} = 0.0097, wR_{all} = 0.0249
Extinction coefficient	0.0232(17)
Largest diff. peak and hole	0.510 and -0.559 e·$Å^{-3}$

$R = \Sigma||F_o|-|F_c|| / \Sigma|F_o|$, $wR = \{\Sigma[w(|F_o|^2 - |F_c|^2)^2] / \Sigma[w(|F_o|^4)]\}^{1/2}$ and $w=1/[\sigma^2(Fo^2)+(0.0185P)^2]$ where $P=(Fo^2+2Fc^2)/3$

Table S2. Atomic coordinates (x 10^4) and equivalent isotropic displacement parameters ($Å^2x10^3$) for $AgSnSe_2$ at 296.7(6) K with estimated standard deviations in parentheses.

Label	x	y	z	Occupancy	U_{eq}^*
Se(1)	5000	10000	0	1	16(1)
Sn(1)	0	5000	5000	0.5002	18(1)
Ag(1)	0	5000	5000	0.5002	18(1)

*U_{eq} is defined as one third of the trace of the orthogonalized U_{ij} tensor.

Table S3. Anisotropic displacement parameters ($Å^2x10^3$) for Ag Se2 Sn at 296.7(6) K with estimated standard deviations in parentheses.

Label	U_{11}	U_{22}	U_{33}	U_{12}	U_{13}	U_{23}
Se(1)	16(1)	16(1)	16(1)	0	0	0
Sn(1)	18(1)	18(1)	18(1)	0	0	0
Ag(1)	18(1)	18(1)	18(1)	0	0	0

The anisotropic displacement factor exponent takes the form: $-2\pi^2[h^2a^{*2}U_{11} + ... + 2hka^*b^*U_{12}]$.

Table S4. Bond lengths [Å] for $AgSnSe_2$ at 296.7(6) K with estimated standard deviations in parentheses.

Label	Distances
Se(1)-Sn(1)	2.84135(10)
Se(1)-Sn(1)	2.84135(10)
Se(1)-Sn(1)	2.84135(10)
Se(1)-Sn(1)	2.84135(10)
Se(1)-Sn(1)	2.84135(10)
Se(1)-Sn(1)	2.84135(10)
Se(1)-Ag(1)	2.84135(10)

Table S5. Crystal data and structure refinement for $AgSb_{0.50}Sn_{0.50}Se_2$ at 295.6(5) K.

Empirical formula	$AgSb_{0.50}Sn_{0.50}Se_2$
Formula weight	386.01
Temperature	295.6(5) K
Wavelength	0.71073 Å
Crystal system	Cubic
Space group	*Fm*-3*m*
Unit cell dimensions	a = 5.74720(10) Å, α = 90° b = 5.74720(10) Å, β = 90° c = 5.74720(10) Å, γ = 90°
Volume	189.832(10) $Å^3$
Z	2
Density (calculated)	6.753 g/cm^3
Absorption coefficient	30.917 mm^{-1}
F(000)	331
Crystal size	0.06 x 0.05 x 0.04 mm^3
θ range for data collection	6.148 to 37.968°
Index ranges	-9<=h<=9, -9<=k<=9, -9<=l<=9
Reflections collected	707
Independent reflections	42 [R_{int} = 0.0194]
Completeness to θ = 25.242°	100%
Refinement method	Full-matrix least-squares on F^2
Data / restraints / parameters	42 / 0 / 4
Goodness-of-fit	1.353
Final R indices [I > 2σ(I)]	R_{obs} = 0.0122, wR_{obs} = 0.0310
R indices [all data]	R_{all} = 0.0122, wR_{all} = 0.0310
Extinction coefficient	0.0076(9)
Largest diff. peak and hole	0.941 and -0.408 e·$Å^{-3}$

$R = \Sigma||F_o|-|F_c|| / \Sigma|F_o|$, $wR = \{\Sigma[w(|F_o|^2 - |F_c|^2)^2] / \Sigma[w(|F_o|^4)]\}^{1/2}$ and $w=1/[\sigma^2(Fo^2)+(0.0130P)^2+0.6593P]$ where $P=(Fo^2+2Fc^2)/3$

Table S6. Atomic coordinates ($x10^4$) and equivalent isotropic displacement parameters ($Å^2x10^3$) for $AgSb_{0.50}Sn_{0.50}Se_2$ at 295.6(5) K with estimated standard deviations in parentheses.

Label	x	y	z	Occupancy	U_{eq}^*
Ag(1)	10000	5000	5000	0.5002	26(1)
Se(1)	5000	5000	5000	1	28(1)
Sn(1)	10000	5000	5000	0.2501	26(1)
Sb(1)	10000	5000	5000	0.2501	26(1)

$^*U_{eq}$ is defined as one third of the trace of the orthogonalized U_{ij} tensor.

Table S7. Anisotropic displacement parameters ($Å^2x10^3$) for $AgSb_{0.50}Sn_{0.50}Se_2$ at 295.6(5) K with estimated standard deviations in parentheses.

Label	U_{11}	U_{22}	U_{33}	U_{12}	U_{13}	U_{23}
Ag(1)	26(1)	26(1)	26(1)	0	0	0
Se(1)	28(1)	28(1)	28(1)	0	0	0
Sn(1)	26(1)	26(1)	26(1)	0	0	0
Sb(1)	26(1)	26(1)	26(1)	0	0	0

The anisotropic displacement factor exponent takes the form: $-2\pi^2[h^2a^{*2}U_{11} + ... + 2hka^*b^*U_{12}]$.

Table S8. Bond lengths [Å] for $AgSb_{0.50}Sn_{0.50}Se_2$ at 295.6(5) K with estimated standard deviations in parentheses.

Label	Distances
Ag(1)-Se(1)	2.87360(5)
Ag(1)-Se(1)	2.87360(5)
Ag(1)-Se(1)	2.87360(5)
Ag(1)-Se(1)	2.87360(5)
Ag(1)-Se(1)	2.87360(5)
Ag(1)-Se(1)	2.87360(5)

Table S9. Fitting parameters for the Sn 3d, Ag 3d and Se 3d XPS spectra of $AgSnSe_2$ $BE_{5/2}$ = binding energy of $3d_{5/2}$, FWHM fit parameter is full width at half maximum, L/G Mix(%) Product is Lorentzian/Gaussian Mix Product.

Orbital (3d)	**$BE_{5/2}$ (eV)**	**FWHM fit parameter (eV)**	**L/G Mix (%) Product**
Ag	367.86	1.07	30
Sn	486.03	1.56	30
Se	53.75	1.29	30

Table S10. Mössbauer hyperfine parameters as resulting from the best fits of the corresponding spectra of the $AgSn_{1-x}Sb_xSe_2$ (x = 0-0.9) samples recorded at 80 K. IS is the isomer shift relative to SnO_2 at 300 K, Γ/2 is the half line-width and AA is the relative spectral absorption area of each component used to fit the spectra. Typical errors are ± 0.02 mm/s for IS and Γ/2 and ± 5% for Area. The values for the x=0 sample are given for both the one-component and three-components fits.

		IS				**Γ/2**				**AA**		
x		**Sn^{4+}**	**Sn^{2+}**	**Sn^{3+}**		**Sn^{4+}**	**Sn^{2+}**	**Sn^{3+}**		**Sn^{4+}**	**Sn^{2+}**	**Sn^{3+}**
0				2.72				0.58				1.00
0		2.51	2.92	2.72		0.51	0.51	0.58		0.10	0.10	0.80
0.1		2.33	2.90	2.72		0.63	0.63	0.58		0.16	0.16	0.68
0.2		2.16	3.17	2.72		0.69	0.69	0.58		0.21	0.24	0.55
0.3		2.12	3.31	2.72		0.58	0.49	0.58		0.31	0.29	0.40
0.4		2.05	3.35	2.72		0.55	0.46	0.58		0.41	0.29	0.30
0.5		2.02	3.42	2.72		0.52	0.49	0.59		0.45	0.40	0.15
0.7		2.02	3.42	2.72		0.52	0.49	0.59		0.50	0.47	0.03
0.8		1.78	3.49			0.42	0.49			0.52	0.48	
0.9		1.69	3.61			0.51	0.56			0.43	0.57	

Table S11. Bader charge analysis of SnSe, $AgSnSe_2$ and $SnSe_2$.

	Avg. Sn charge	**Avg. Se charge**	**Avg. Ag charge**
SnSe	0.83	-0.83	-
$AgSnSe_2$	0.95	-0.63	0.31
$SnSe_2$	1.19	-0.59	-

Table S12. Binomial probabilities of finding n out of 12 first Sn cationic neighbours to a Sn site, as a function of the Sb concentration x in $AgSn_{1-x}Sb_xSe_2$.

		n											
x	0	1	2	3	4	5	6	7	8	9	10	11	12
0	0.000	0.003	0.016	0.054	0.121	0.193	0.226	0.193	0.121	0.054	0.016	0.003	0.000
0.1	0.001	0.008	0.034	0.092	0.170	0.222	0.212	0.149	0.076	0.028	0.007	0.001	0.000
0.2	0.002	0.017	0.064	0.142	0.213	0.227	0.177	0.101	0.042	0.012	0.002	0.000	0.000
0.3	0.006	0.037	0.109	0.195	0.237	0.204	0.128	0.059	0.020	0.005	0.001	0.000	0.000
0.4	0.014	0.071	0.168	0.240	0.231	0.158	0.079	0.029	0.008	0.001	0.000	0.000	0.000
0.5	0.032	0.127	0.232	0.258	0.194	0.103	0.040	0.011	0.002	0.000	0.000	0.000	0.000
0.6	0.069	0.206	0.283	0.236	0.133	0.053	0.016	0.003	0.001	0.000	0.000	0.000	0.000
0.7	0.142	0.301	0.292	0.172	0.068	0.019	0.004	0.001	0.000	0.000	0.000	0.000	0.000
0.8	0.282	0.377	0.230	0.085	0.021	0.004	0.000	0.000	0.000	0.000	0.000	0.000	0.000
0.9	0.540	0.341	0.099	0.017	0.002	0.000	0.000	0.000	0.000	0.000	0.000	0.000	0.000
1	1.000	0.000	0.000	0.000	0.000	0.000	0.000	0.000	0.000	0.000	0.000	0.000	0.000

Table S13. Total binomial probabilities of finding at least m and up to 12 first Sn cationic neighbours to a Sn site, as a function of the Sb concentration x in $AgSn_{1-x}Sb_xSe_2$.

	at least m											
x	1	2	3	4	5	6	7	8	9	10	11	12
0	1.000	0.997	0.981	0.927	0.806	0.613	0.387	0.194	0.073	0.019	0.003	0.000
0.1	0.999	0.992	0.958	0.866	0.696	0.473	0.261	0.112	0.036	0.008	0.001	0.000
0.2	0.998	0.980	0.917	0.775	0.562	0.335	0.158	0.057	0.015	0.003	0.000	0.000
0.3	0.994	0.958	0.849	0.653	0.417	0.213	0.085	0.026	0.006	0.001	0.000	0.000
0.4	0.986	0.915	0.747	0.507	0.276	0.118	0.039	0.009	0.002	0.000	0.000	0.000
0.5	0.968	0.842	0.609	0.351	0.158	0.054	0.014	0.003	0.000	0.000	0.000	0.000
0.6	0.931	0.725	0.442	0.205	0.073	0.019	0.004	0.001	0.000	0.000	0.000	0.000
0.7	0.858	0.557	0.264	0.092	0.024	0.005	0.001	0.000	0.000	0.000	0.000	0.000
0.8	0.718	0.341	0.111	0.026	0.004	0.001	0.000	0.000	0.000	0.000	0.000	0.000
0.9	0.460	0.118	0.020	0.002	0.000	0.000	0.000	0.000	0.000	0.000	0.000	0.000
1	0.000	0.000	0.000	0.000	0.000	0.000	0.000	0.000	0.000	0.000	0.000	0.000

Table S14. Fitting parameters of Sn K-Edge k^2-weighted EXAFS spectra for $AgSnSe_2$ sample.

Path	R (Å)	N	(σ^2)	S_0^2	ΔE (eV)	R - factor
Sn-Se	2.40 ± 0.04	4.74 ± 0.17	0.011 ± 0.001	0.796 ± 0.170	4.03 ± 2.08	0.035
Sn-Sn	3.82 ± 0.02	9.52 ± 0.42	0.021 ± 0.006	1.193 ± 0.427	5.860 ± 1.674	

Table S15. *p*-type carrier concentration (n) of $AgSn_{1-x}Sb_xSe_2$ (x = 0-0.99) samples at 300 K.

Sample	***n* (cm^{-3})**
$AgSnSe_2$	$2.4 \pm 0.2 \times 10^{22}$
$AgSn_{0.9}Sb_{0.1}Se_2$	$2.0 \pm 0.3 \times 10^{22}$
$AgSn_{0.8}Sb_{0.2}Se_2$	2.00×10^{22}
$AgSn_{0.5}Sb_{0.5}Se_2$	$5.5 \pm 0.3 \times 10^{21}$
$AgSn_{0.3}Sb_{0.7}Se_2$	4.00×10^{19}
$AgSn_{0.01}Sb_{0.99}Se_2$	$4.0 \pm 1.0 \times 10^{17}$

Table S16. Oxidation states of Sn and corresponding electrical conductivity values for selected Sn-based chalcogenides.

Sample	**Oxidation state**	**Electrical conductiivty (S/cm) at 300 K**	**Ref.**
SnSe	+2	1.18	[48]
$AgSnSe_2$	+3	3056	**This work**
$AgSn_{0.5}Sb_{0.5}Se_2$	+2 and +4	205	**This work**
$SnSe_2$	+4	0.85	[49]

Table S17. Parameters obtained from the fitting of low-temperature C_p/T vs. T^2 data of $AgSnSe_2$ using a Debye-Einstein model with three Einstein oscillators

Parameter	Value
γ (J/mole.K^2)	5.7 x 10^{-3}
θ_D (K)	202
θ_{E1} (K)	122
θ_{E2} (K)	23
θ_{E3} (K)	62

Table S18. Density of $AgSn_{1-x}Sb_xSe_2$ (x = 0-0.99) samples

Sample	Density (g/cc)
$AgSnSe_2$	6.20
$AgSn_{0.9}Sb_{0.1}Se_2$	5.90
$AgSn_{0.8}Sb_{0.2}Se_2$	5.47
$AgSn_{0.7}Sb_{0.3}Se_2$	5.39
$AgSn_{0.6}Sb_{0.4}Se_2$	5.49
$AgSn_{0.5}Sb_{0.5}Se_2$	5.80
$AgSn0._3Sb0._7Se_2$	5.90
$AgSn0._2Sb0._8Se_2$	5.71
$AgSn_{0.01}Sb_{0.99}Se_2$	6.00

References

1 Sheldrick, G. M. SHELXT–Integrated space-group and crystal-structure determination. *Foundations of Crystallography* **71**, 3-8 (2015).

2 Dolomanov, O. V., Bourhis, L. J., Gildea, R. J., Howard, J. A. & Puschmann, H. OLEX2: a complete structure solution, refinement and analysis program. *Applied Crystallography* **42**, 339-341 (2009).

3 Sheldrick, G. M. Crystal structure refinement with SHELXL. *Crystal Structure Communications* **71**, 3-8 (2015).

4 Roisnel, T., Rodríguez-Carvajal, J. & Gonzalez-Platas, J. in *Mater. Sci. Forum.* 118-123.

5 Juhas, P., Davis, T., Farrow, C. L. & Billinge, S. J. L. PDFgetX3: a rapid and highly automatable program for processing powder diffraction data into total scattering pair distribution functions. *Journal of Applied Crystallography* **46**, 560-566 (2013). https://doi.org:doi:10.1107/S0021889813005190

6 Farrow, C. L., Juhas, P., Liu, J. W., Bryndin, D., Božin, E. S., Bloch, J., Proffen, T. & Billinge, S. J. L. PDFfit2 and PDFgui: computer programs for studying nanostructure in crystals. *Journal of Physics: Condensed Matter* **19**, 335219 (2007). https://doi.org:10.1088/0953-8984/19/33/335219

7 Douvalis, A., Polymeros, A. & Bakas, T. in *Journal of Physics: Conference Series.* 012014 (IOP Publishing).

8 Nasredinov, F. S., Nemov, S. A., Masterov, V. F. & Seregin, P. P. Mössbauer studies of negative-U tin centers in lead chalcogenides. *Physics of the Solid State* **41**, 1741-1758 (1999). https://doi.org:10.1134/1.1131091

9 Oudah, M., Takegami, D., Kitao, S., Lado, J. L., Meléndez-Sans, A., Christovam, D. S., Yoshimura, M., Tsuei, K.-D., McNally, G., Isobe, M., Küster, K., Seto, M., Keimer, B., Bonn, D. A., Tjeng, L. H., Sawatzky, G. & Takagi, H. Charge-entropy-stabilized selenide $Ag_xSn_{1-x}Se$. *Communications Materials* **6**, 58 (2025). https://doi.org:10.1038/s43246-025-00778-3

10 Masterov, V., Nasredinov, F., Nemov, S., Seregin, P., Irkaev, S., Melekh, B. & Troitskaya, N. Unconventional tin atom states in mixed silver and tin chalcogenides having NaCl structure. *Physics of the Solid State* **38**, 1805-1806 (1996).

11 Ravel, B. & Newville, M. ATHENA, ARTEMIS, HEPHAESTUS: data analysis for X-ray absorption spectroscopy using IFEFFIT. *Journal of Synchrotron Radiation* **12**, 537-541 (2005). https://doi.org:doi:10.1107/S0909049505012719

12 Jana, M. K., Pal, K., Warankar, A., Mandal, P., Waghmare, U. V. & Biswas, K. Intrinsic Rattler-Induced Low Thermal Conductivity in Zintl Type $TlInTe_2$. *Journal of the American Chemical Society* **139**, 4350-4353 (2017). https://doi.org:10.1021/jacs.7b01434

13 Samanta, M., Pal, K., Pal, P., Waghmare, U. V. & Biswas, K. Localized Vibrations of Bi Bilayer Leading to Ultralow Lattice Thermal Conductivity and High Thermoelectric Performance in Weak Topological Insulator n-Type BiSe. *Journal of the American Chemical Society* **140**, 5866-5872 (2018). https://doi.org:10.1021/jacs.8b02691

14 Kim, H.-S., Gibbs, Z. M., Tang, Y., Wang, H. & Snyder, G. J. Characterization of Lorenz number with Seebeck coefficient measurement. *APL Materials* **3**, 041506 (2015). https://doi.org:10.1063/1.4908244

15 Blöchl, P. E. Projector augmented-wave method. *Physical Review B* **50**, 17953-17979 (1994). https://doi.org:10.1103/PhysRevB.50.17953

16 Kresse, G. & Joubert, D. From ultrasoft pseudopotentials to the projector augmented-wave method. *Physical Review B* **59**, 1758-1775 (1999). https://doi.org:10.1103/PhysRevB.59.1758

17 Perdew, J. P., Ruzsinszky, A., Csonka, G. I., Vydrov, O. A., Scuseria, G. E., Constantin, L. A., Zhou, X. & Burke, K. Restoring the Density-Gradient Expansion for Exchange in Solids and Surfaces. *Physical Review Letters* **100**, 136406 (2008). https://doi.org:10.1103/PhysRevLett.100.136406

18 Perdew, J. P., Burke, K. & Ernzerhof, M. Generalized Gradient Approximation Made Simple. *Physical Review Letters* **77**, 3865-3868 (1996). https://doi.org:10.1103/PhysRevLett.77.3865

19 Kresse, G. & Furthmüller, J. Efficiency of ab-initio total energy calculations for metals and semiconductors using a plane-wave basis set. *Computational Materials Science* **6**, 15-50 (1996). https://doi.org:https://doi.org/10.1016/0927-0256(96)00008-0

20 Kresse, G. & Furthmüller, J. Efficient iterative schemes for ab initio total-energy calculations using a plane-wave basis set. *Physical Review B* **54**, 11169-11186 (1996). https://doi.org:10.1103/PhysRevB.54.11169

21 Ångqvist, M., Muñoz, W. A., Rahm, J. M., Fransson, E., Durniak, C., Rozyczko, P., Rod, T. H. & Erhart, P. ICET – A Python Library for Constructing and Sampling Alloy Cluster Expansions. *Advanced Theory and Simulations* **2**, 1900015 (2019). https://doi.org:https://doi.org/10.1002/adts.201900015

22 Jia, B., Wu, D., Xie, L., Wang, W., Yu, T., Li, S., Wang, Y., Xu, Y., Jiang, B., Chen, Z., Weng, Y. & He, J. Pseudo-nanostructure and trapped-hole release induce high thermoelectric performance in PbTe. *Science* **384**, 81-86 (2024). https://doi.org:10.1126/science.adj8175

23 Roychowdhury, S., Ghosh, T., Arora, R., Samanta, M., Xie, L., Singh, N. K., Soni, A., He, J., Waghmare, U. V. & Biswas, K. Enhanced atomic ordering leads to high thermoelectric performance in $AgSbTe_2$. *Science* **371**, 722-727 (2021). https://doi.org:10.1126/science.abb3517

24 Shi, X.-L., Zou, J. & Chen, Z.-G. Advanced Thermoelectric Design: From Materials and Structures to Devices. *Chemical Reviews* **120**, 7399-7515 (2020). https://doi.org:10.1021/acs.chemrev.0c00026

25 Xiao, Y. & Zhao, L.-D. Seeking new, highly effective thermoelectrics. *Science* **367**, 1196-1197 (2020). https://doi.org:10.1126/science.aaz9426

26 Xu, S., Horta, S., Lawal, A., Maji, K., Lorion, M. & Ibáñez, M. Interfacial bonding enhances thermoelectric cooling in 3D-printed materials. *Science* **387**, 845-850 (2025). https://doi.org:10.1126/science.ads0426

27 Yan, Q. & Kanatzidis, M. G. High-performance thermoelectrics and challenges for practical devices. *Nature Materials* **21**, 503-513 (2022). https://doi.org:10.1038/s41563-021-01109-w

28 Ren, Z., Kriener, M., Taskin, A. A., Sasaki, S., Segawa, K. & Ando, Y. Anomalous metallic state above the upper critical field of the conventional three-dimensional superconductor $AgSnSe_2$ with strong intrinsic disorder. *Physical Review B* **87**, 064512 (2013). https://doi.org:10.1103/PhysRevB.87.064512

29 Huo, H., Zhang, Y., Guo, K., Yang, X., Xing, J., Li, S., Zhang, J. & Luo, J. Improvement of anisotropic thermoelectric performance in polycrystalline SnSe by metallic $AgSnSe_2$ compositing. *Journal of Alloys and Compounds* **908**, 164649 (2022). https://doi.org:https://doi.org/10.1016/j.jallcom.2022.164649

30 Niu, X., Lang, Y., Pan, L. & Wang, Y. Effects of $AgSnSe_2$ addition on the thermoelectric properties of $Bi_{0.5}Sb_{1.5}Te_3$. *Journal of Alloys and Compounds* **956**, 170399 (2023). https://doi.org:https://doi.org/10.1016/j.jallcom.2023.170399

31 Liang, G., Lyu, T., Hu, L., Qu, W., Zhi, S., Li, J., Zhang, Y., He, J., Li, J., Liu, F., Zhang, C., Ao, W., Xie, H. & Wu, H. $(GeTe)_{1-x}(AgSnSe_2)_x$: Strong Atomic Disorder-Induced High Thermoelectric Performance near the Ioffe–Regel Limit. *ACS Applied Materials & Interfaces* **13**, 47081-47089 (2021). https://doi.org:10.1021/acsami.1c14801

32 Liu, C., Huang, Z., Wang, D., Wang, X., Miao, L., Wang, X., Wu, S., Toyama, N., Asaka, T., Chen, J., Nishibori, E. & Zhao, L.-D. Dynamic Ag^+-intercalation with $AgSnSe_2$ nano-precipitates in Cl-doped polycrystalline $SnSe_2$ toward ultra-high thermoelectric performance. *Journal of Materials Chemistry A* **7**, 9761-9772 (2019). https://doi.org:10.1039/C9TA01678C

33 Song, S., Tseng, Y.-C. & Mozharivskyj, Y. Optimizing thermoelectric performance of SnTe via alloying with $AgSnSe_2$ and PbTe. *Journal of Alloys and Compounds* **947**, 169415 (2023). https://doi.org:https://doi.org/10.1016/j.jallcom.2023.169415

34 Pan, L., Mitra, S., Zhao, L.-D., Shen, Y., Wang, Y., Felser, C. & Berardan, D. The Role of Ionized Impurity Scattering on the Thermoelectric Performances of Rock Salt $AgPb_mSnSe_{2+m}$. *Advanced Functional Materials* **26**, 5149-5157 (2016). https://doi.org:https://doi.org/10.1002/adfm.201600623

35 Dutta, M., Prasad, M. V. D., Pandey, J., Soni, A., Waghmare, U. V. & Biswas, K. Local Symmetry Breaking Suppresses Thermal Conductivity in Crystalline Solids. *Angewandte Chemie International Edition* **61**, e202200071 (2022). https://doi.org:https://doi.org/10.1002/anie.202200071

36 Morelli, D. T., Jovovic, V. & Heremans, J. P. Intrinsically Minimal Thermal Conductivity in Cubic I-V-VI_2 Semiconductors. *Physical Review Letters* **101**, 035901 (2008). https://doi.org:10.1103/PhysRevLett.101.035901

37 Pan, L., Bérardan, D. & Dragoe, N. High Thermoelectric Properties of n-Type $AgBiSe_2$. *Journal of the American Chemical Society* **135**, 4914-4917 (2013). https://doi.org:10.1021/ja312474n

38 Hua, X., I. Hegde, V. & Wolverton, C. Phase Stability and Ordering in Rock Salt-Based Thermoelectrics: $NaSbX_2$, $AgSbX_2$, and Their Alloys with PbX and SnX (X = S, Se, Te). *Chemistry of Materials* **31**, 9445-9452 (2019). https://doi.org:10.1021/acs.chemmater.9b03318

39 Geller, S. & Wernick, J. H. Ternary semiconducting compounds with sodium chloride-like structure: $AgSbSe_2$, $AgSbTe_2$, $AgBiS_2$, $AgBiSe_2$. *Acta Crystallographica* **12**, 46-54 (1959). https://doi.org:doi:10.1107/S0365110X59000135

40 Guin, S. N., Chatterjee, A., Negi, D. S., Datta, R. & Biswas, K. High thermoelectric performance in tellurium free p-type $AgSbSe_2$. *Energy & Environmental Science* **6**, 2603-2608 (2013). https://doi.org:10.1039/C3EE41935E

41 Wojciechowski, K., Schmidt, M., Tobola, J., Koza, M., Olech, A. & Zybała, R. Influence of Doping on Structural and Thermoelectric Properties of $AgSbSe_2$. *Journal of Electronic Materials* **39**, 2053-2058 (2010). https://doi.org:10.1007/s11664-009-1008-8

42 Acharyya, P., Das, A., Arora, R., Samanta, M., Das, S., Ghosh, T., Waghmare, U. V. & Biswas, K. Electronic Structure Modulation in GeTe by Hg and Sb Codoping Leads to High Thermoelectric Performance. *Journal of the American Chemical Society* **147**, 19296-19304 (2025). https://doi.org:10.1021/jacs.5c05116

43 Lin, W., He, J., Su, X., Zhang, X., Xia, Y., Bailey, T. P., Stoumpos, C. C., Tan, G., Rettie, A. J. E., Chung, D. Y., Dravid, V. P., Uher, C., Wolverton, C. & Kanatzidis, M. G. Ultralow Thermal Conductivity, Multiband Electronic Structure and High Thermoelectric Figure of Merit in TlCuSe. *Advanced Materials* **33**, 2104908 (2021). https://doi.org:https://doi.org/10.1002/adma.202104908

44 Ghosh, T., Dutta, M., Sarkar, D. & Biswas, K. Insights into Low Thermal Conductivity in Inorganic Materials for Thermoelectrics. *Journal of the American Chemical Society* **144**, 10099-10118 (2022). https://doi.org:10.1021/jacs.2c02017

45 Das, A., Pal, K., Acharyya, P., Das, S., Maji, K. & Biswas, K. Strong Antibonding I (p)–Cu (d) States Lead to Intrinsically Low Thermal Conductivity in $CuBiI_4$. *Journal of the American Chemical Society* **145**, 1349-1358 (2023). https://doi.org:10.1021/jacs.2c11908

46 Mukhopadhyay, S., Parker, D. S., Sales, B. C., Puretzky, A. A., McGuire, M. A. & Lindsay, L. Two-channel model for ultralow thermal conductivity of crystalline Tl_3VSe_4. *Science* **360**, 1455 (2018). https://doi.org:10.1126/science.aar8072

47 Dutta, M., Matteppanavar, S., Prasad, M. V. D., Pandey, J., Warankar, A., Mandal, P., Soni, A., Waghmare, U. V. & Biswas, K. Ultralow Thermal Conductivity in Chain-like TlSe Due to Inherent Tl^+ Rattling. *Journal of the American Chemical Society* **141**, 20293-20299 (2019). https://doi.org:10.1021/jacs.9b10551

48 Chandra, S., Arora, R., Waghmare, U. V. & Biswas, K. Modulation of the electronic structure and thermoelectric properties of orthorhombic and cubic SnSe by $AgBiSe_2$ alloying. *Chemical Science* **12**, 13074-13082 (2021). https://doi.org:10.1039/D1SC03696C

49 Zhou, C., Yu, Y., Zhang, X., Cheng, Y., Xu, J., Lee, Y. K., Yoo, B., Cojocaru-Mirédin, O., Liu, G., Cho, S.-P., Wuttig, M., Hyeon, T. & Chung, I. Cu Intercalation and Br Doping to Thermoelectric $SnSe_2$ Lead to Ultrahigh Electron Mobility and Temperature-Independent Power Factor. *Advanced Functional Materials* **30**, 1908405 (2020). https://doi.org:https://doi.org/10.1002/adfm.201908405